

This is the accepted manuscript made available via CHORUS, the article has been published as:

# Homoclinic snaking near a codimension-two Turing-Hopf bifurcation point in the Brusselator model

J. C. Tzou, Y.-P. Ma, A. Bayliss, B. J. Matkowsky, and V. A. Volpert

Phys. Rev. E **87**, 022908 — Published 14 February 2013

DOI: [10.1103/PhysRevE.87.022908](https://doi.org/10.1103/PhysRevE.87.022908)

# HOMOCLINIC SNAKING NEAR A CODIMENSION TWO TURING-HOPF BIFURCATION POINT IN THE BRUSSELATOR MODEL

J. C. TZOU<sup>1,\*</sup>, Y. -P. MA<sup>1,2,\*</sup>, A. BAYLISS<sup>1</sup>, B. J. MATKOWSKY<sup>1,\*</sup>, AND V. A. VOLPERT<sup>1</sup>

**ABSTRACT.** Spatiotemporal Turing-Hopf pinning solutions near the codimension two Turing-Hopf point of the one-dimensional Brusselator model are studied. Both the Turing and Hopf bifurcations are supercritical and stable. The pinning solutions exhibit coexistence of stationary stripes of near critical wavelength and time periodic oscillations near the characteristic Hopf frequency. Such solutions of this nonvariational problem are in contrast to the stationary pinning solutions found in the subcritical Turing regime for the variational Swift-Hohenberg equations, characterized by a spatially periodic pattern embedded in a spatially homogeneous background state. Numerical continuation was used to solve periodic boundary value problems in time for the Fourier amplitudes of the spatiotemporal Turing-Hopf pinning solutions. The solution branches are organized in a series of saddle-node bifurcations similar to the known snaking structures of stationary pinning solutions. We find two intertwined pairs of such branches, one with a defect in the middle of the striped region, and one without. Solutions on one branch of one pair differ from those on the other branch by a  $\pi$  phase shift in the spatially periodic region, i.e., locations of local minima of solutions on one branch correspond to locations of maxima of solutions on the other branch. These branches are connected to branches exhibiting collapsed snaking behavior, where the snaking region collapses to almost a single value in the bifurcation parameter. Solutions along various parts of the branches are described in detail. Time dependent depinning dynamics outside the saddle-nodes are illustrated, and a time scale for the depinning transitions is numerically established. Wavelength variation within the snaking region is discussed, and reasons for the variation are given in the context of amplitude equations. Finally, we compare the pinning region to the Maxwell line found numerically by time evolving the amplitude equations.

**Key words:** homoclinic snaking, weakly nonlinear regime, codimension two Turing-Hopf bifurcation point, localized patterns.

## 1 Introduction

Localized stationary solutions of reaction-diffusion systems characterized by the coexistence of a flat, i.e., stationary (time independent), spatially homogeneous state with a spatially periodic state have recently been the subject of much analysis. In the context of variational systems, a stationary front between two stationary states is expected when both states possess equal free energy. The point (or curve) in parameter space at which the free energies are equal is referred to as a Maxwell point (curve). When the coexistence is between two flat states, a perturbation from the Maxwell point results in a time dependent invasion of the energetically favored state into the other. In [1], Pomeau explains that when the coexistence is between a flat and spatially

---

<sup>1</sup>DEPT. OF ENGINEERING SCIENCES AND APPLIED MATHEMATICS, NORTHWESTERN UNIVERSITY, 2145 SHERIDAN ROAD, EVANSTON, IL, 60208 USA

<sup>2</sup>DEPT. OF GEOPHYSICAL SCIENCES, UNIVERSITY OF CHICAGO, 5734 S. ELLIS AVENUE, CHICAGO, IL, 60637 USA

\* CORRESPONDING AUTHORS

*E-mail address:* tzou.justin@gmail.com, yiping.m@gmail.com, b-matkowsky@northwestern.edu.

periodic state, there is a broadening of the Maxwell point. Thus, within a finite-width region in parameter space around the Maxwell point, a continuum of such solutions exist. The broadening of the Maxwell point may be explained by the fact that the energy difference must be sufficiently large in order to displace the front connecting the coexisting states by one wavelength of the periodic pattern. Equivalently, displacement of the front only occurs sufficiently far from the Maxwell point. This effect has been referred to (e.g., [2] and references therein) as the pinning of the spatially periodic front. By assembling two such fronts back-to-back, one can construct stationary solutions in which a finite region of spatially periodic states is embedded in a background of flat state. Such solutions are known as spatially localized states in a broader context (cf. [3]). These include for example the experimental observations of stationary two-dimensional radially symmetric ‘solitons’ in a ferrofluid with an external magnetic field applied vertically (cf. [4]), and one-dimensional localized patterns in a nematic liquid crystal layer with a spatially modulated optical feedback (cf. [5]). The properties of the latter were shown to be consistent with previous theoretical work on stationary pinning solutions in pattern forming PDEs, which we shall review next. The pinning phenomenon is explained in detail in [1].

The (variational) 2–3 and 3–5 Swift-Hohenberg equations for a real scalar field  $u(x, t)$ , which exhibit quadratic–cubic, and cubic–quintic nonlinearities, respectively, have been studied extensively to illustrate the phenomenon of pinning. Most of these studies have focused on the subcritical Turing regime where there is bistability between the flat and spatially periodic states. In [6] for the 2–3 Swift-Hohenberg equation on an unbounded domain, a continuum of pinning solutions was shown to exist on branches that “snake” back and forth in the bifurcation diagram forming a series of saddle-node bifurcations. As predicted in [1], the snaking region was found to straddle the Maxwell point. Solutions on these branches are even in space and thus preserve the spatial reversibility symmetry ( $x \rightarrow -x, u \rightarrow u$ ) of the 2–3 Swift-Hohenberg equation. The snaking region consists of two intertwined branches, with solutions on one branch having a local maximum in the central part of the spatially periodic region, and solutions on the other branch having a local minimum. Solutions at different points along one branch differ in the width of the spatially periodic region. In particular, traversal through two saddle-nodes or equivalently one back and forth cycle on the snaking branch corresponds to two wavelengths of the spatially periodic state being added or subtracted at the edges of the spatially periodic region. In [2] it was found that in addition to the two snaking branches of symmetric solutions, a series of pitchfork bifurcations near the saddle-nodes on these branches are connected through a series of rungs (or ladders) of asymmetric solutions. The entire bifurcation diagram of stationary pinning solutions was therefore dubbed snakes-and-ladders. Outside the snaking region, a depinning transition was shown to occur in which wavelengths were either nucleated or destroyed at the edges of the spatially periodic region. The speed of depinning was calculated analytically and confirmed numerically. The conservation of a spatial Hamiltonian was shown to select the wavelength of the spatially periodic state within the snaking region, and the wavelength variation across the snaking region was qualitatively explained based on the free energy variation of the flat and spatially periodic states. Studies of stationary pinning solutions whose analogs are not addressed in these papers include the effects of finite domain lengths on snaking. In [7], it was shown that snaking branches in a spatially periodic domain terminate on branches of spatially periodic states whose wavenumber depends on the domain length. It was also determined that these termination points corresponded to the Eckhaus instability boundary. In [8], it was found that non-periodic and non-Neumann

boundary conditions eliminated entirely spatially periodic states of the Swift-Hohenberg equation, replacing them with states with defects at or near the boundary. In this case, instead of terminating on spatially periodic branches, the snaking branches either exit the snaking region and develop into branches of large amplitude patterns, or they may turn back toward small amplitude and terminate at other primary bifurcation points on the flat state. In [9], a multiple scale analysis was used to derive an envelope equation for pinning solutions of the non-symmetric generalized Swift-Hohenberg equation. More recently, the entire snakes-and-ladders bifurcation diagram, including in particular the width of the pinning region, was constructed through a multiple scale analysis beyond all algebraic orders for the 2–3 Swift Hohenberg equation near the onset of subcriticality (cf. [10]). Subsequently, a considerably simpler construction using a variational approximation was proposed (cf. [11]). For the 3–5 Swift-Hohenberg equation, the additional up-down symmetry ( $x \rightarrow x, u \rightarrow -u$ ) admits two additional snaking branches of odd solutions (cf. [12, 13]). In contrast to the 2–3 case, traversal through four saddle-nodes on one snaking branch is required to add two wavelengths at the edges of the spatially periodic region in the 3–5 Swift-Hohenberg equation (cf. [14]).

Another explanation for the existence of stationary pinning solutions has been given in terms of reversible spatial dynamics (see e.g., [12, 15–17], or [18–21] for spike patterns in singularly perturbed reaction-diffusion systems). In this framework, the locations in the complex plane of the spatial eigenvalues (in the case of flat states) or spatial Floquet multipliers (in the case of spatially periodic states), along with spatial reversibility are the key components responsible for the existence of pinning solutions. The most complete account to date of the snakes-and-ladders bifurcation diagram from this perspective can be found in [22], which formulated a set of hypotheses about the connecting orbit between the flat and spatially periodic states that guarantees snaking. Whereas the free-energy description is limited only to pinning solutions of variational systems, the spatial dynamics framework extends the theory of pinning to a much broader class of systems. In particular, a cubic-quintic Ginzburg-Landau equation can be derived as a truncated normal form near weakly subcritical Turing bifurcations, and its solutions yield insights into the location of the pinning region in both variational and nonvariational systems. While no true snaking is possible in this equation due to phase rotation symmetry of the spatial dynamical system, branches emanating from Eckhaus bifurcation points exhibiting snake-like behavior (termed “protosnaking”) were found near the nonvariational analog of the Maxwell point (cf. [23]). Stationary pinning solutions organized along snaking branches have indeed been observed in many nonvariational systems. In [24], two snaking branches were computed for the Lugiato-Lefever equation; in addition, it was shown that there are other pinning solutions found by directly computing the invariant manifolds to the flat and spatially periodic states. A study of a nonvariational extension of the 3–5 Swift-Hohenberg equation in [25] stressed that asymmetric pinning solutions on the ladders are expected to travel in nonvariational systems. In [17], the forced complex Ginzburg-Landau equations were shown to exhibit a different growth mechanism by which periodic structures were nucleated or destroyed in the middle of the spatially periodic region as opposed to the edges. In this case the codimension-two point marking the onset of snaking corresponds to the simultaneous occurrence of a (codimension-one) heteroclinic orbit between two inequivalent flat states and a (codimension-one) supercritical Turing bifurcation on one of them. Hence the nature of the bistability between flat and spatially periodic states in this study differs from the aforementioned studies that mainly focused on subcritical Turing bifurcations.

Nonvariational systems allow for temporal oscillations, which have not been considered in the context of snaking structures of pinning solutions. In particular, pinning solutions characterized by a coexistence of

Turing and Hopf states have been observed in [26] in the vicinity of a codimension two Turing-Hopf point (C2THP) of the (nonvariational) Brusselator model (see e.g., [27–29] and the references therein), where both the Turing and Hopf bifurcations were supercritical and stable. Turing-Hopf coexistence has also been observed experimentally, as in [30] for the voltages and currents of resistively coupled nonlinear LC oscillators arranged in a one-dimensional chain and driven by a constant voltage at one end. Depending on experimental parameter values, it was found that a front connecting a Turing domain to a Hopf domain could propagate in either direction or remain stationary. The same behavior was also observed numerically in the continuous reaction-diffusion approximation of the oscillator chain for parameter values near the C2THP. In another experiment involving convection of a binary fluid in an annular container (cf. [31]), stationary convective rolls were found to coexist with traveling wave bursts, with relative widths of each region depending on the Rayleigh number.

The activator-inhibitor Brusselator model, describing a simplified autocatalytic reaction, has long been a paradigm of nonlinear analysis and is given by

$$u_t = Du_{xx} + E - (B + 1)u + vu^2, \quad x \in \mathbb{R}, \quad t > 0; \quad (1.1a)$$

$$v_t = v_{xx} + Bu - vu^2, \quad x \in \mathbb{R}, \quad t > 0, \quad (1.1b)$$

subject to appropriate initial and boundary conditions. Note that, unlike the Swift-Hohenberg equations, the spatial dynamics of (1.1) are not Hamiltonian. Spatiotemporal patterns near the Brusselator C2THP have also been computed for the superdiffusive variant of (1.1) in [32]. Both of these studies were restricted to using only time evolution techniques to compute the pinning solutions, which only yielded a very narrow view of all possible Turing-Hopf pinning solutions, since only stable solutions can be computed with a standard initial boundary value problem (IBVP) code. Furthermore, the manner in which these solutions are organized on solution branches is difficult to ascertain. In this paper, we use AUTO [33] to solve boundary value problems in time for the  $0, \dots, N$  spatial Fourier amplitudes of the solutions  $u$  and  $v$  to (1.1) for appropriately large  $N$ , under the assumption of spatial periodicity (the  $-N, \dots, -1$  modes are also accounted for since we only consider real solutions). In this way, we obtain both stable and unstable solution branches, and the structure of these branches is readily obtained. Solutions on these branches resemble stationary pinning solutions, only with the flat state replaced by Hopf-like temporal oscillations. The respective growth rates of the Turing and Hopf modes near the C2THP assume the roles of the free energies of the coexisting states in variational systems, with larger growth rates implying greater dominance. While the equality of growth rates is not the analogous Maxwell condition, the “physical” roles of the growth rates and the free energies in the respective systems are analogous. We remark that space-time solutions presented in this paper involve interfaces between regions in space that oscillate in time, and regions that are spatially periodic and stationary in time. Such interfaces cannot be assigned to any of the four classes of defects solutions proposed in [34] for time-periodic solutions of reaction-diffusion systems, as the defects discussed generically serve as interfaces between only traveling waves of nonzero speed.

This paper is organized as follows. In §2, we briefly review the derivation of the amplitude equations near the C2THP of (1.1) and give conditions for Turing-Hopf bistability. These results are used to facilitate a search in parameter space for Turing-Hopf pinning solutions. In §3.1, we describe the equations used to

compute the pinning solutions using the method of continuation in AUTO. We then present in §3.2 the snaking branches on which the pinning solutions exist and discuss their relationship to the pure Turing and pure Hopf branches. We describe the solutions found on these branches and how they vary as the solution branch is traversed. In §3.3, we illustrate the process by which solutions depin when parameters are set a distance  $\delta$  outside of the snaking region, and give a numerical estimate of the scaling of the depinning speed with respect to  $\delta$ . We give a qualitative explanation for the direction of depinning based on the relative dominance of the Turing and Hopf modes. In §3.4, we illustrate the dependence of the wavelength of the spatially periodic state on the parameters of the Brusselator model. In §3.5, we offer an explanation for the observed dependence in the framework of properties of the amplitude equations derived in §2. We then conclude and discuss open problems in §4.

## 2 Turing-Hopf Bistability

In this section, we briefly outline the derivation of the evolution equations for the amplitudes of the Turing and Hopf modes near the C2THP. For a detailed analysis, see [35], or [32] for the superdiffusive variant of Brusselator model. See [36] for a review of normal form theory near the codimension two point, and [29] and [37] for a weakly nonlinear analysis of Turing patterns of the regular and superdiffusive Brusselator models in two dimensions. Stability results from analysis of the amplitude equations will yield the regime of Turing-Hopf bistability in which pinning behavior is possible, as it is in this regime of bistability that the pure Turing and pure Hopf modes may coexist in physical space.

The system (1.1) has one spatially homogeneous steady state  $(u, v)^\top = (E, B/E)^\top$ . Here,  $\top$  denotes the transpose. As  $B$  is increased past  $B_H = 1 + E^2$ , the basic state loses stability through a Hopf bifurcation yielding spatially homogeneous temporal oscillations of frequency  $\omega_c = E$ . As  $B$  is increased past  $B_T = (1 + E\sqrt{D})^2$ , a steady state Turing bifurcation occurs, yielding a stationary spatially periodic pattern with critical wavenumber  $k_c = [E/(\sqrt{1 + E^2} - 1)]^{1/2}$ . When the Hopf and Turing bifurcations occur simultaneously, i.e., when  $B_H = B_T$ , the point in parameter space is referred to as a codimension two Turing-Hopf point. This condition is satisfied when  $D = D_c = [(\sqrt{1 + E^2} - 1)/E]^2$ . To analyze the slow-time evolution of the two modes near the C2THP, we let  $B = B_H + \epsilon^2\mu$  and  $D = D_c + \epsilon^2\rho$ , where  $0 < \epsilon \ll 1$  and  $\mu$  and  $\rho$  are both  $\mathcal{O}(1)$ . When  $\rho > 0$  ( $\rho < 0$ ), the Hopf (Turing) bifurcation is the first to occur as  $B$  is increased. Introducing the slow time scale  $T = \epsilon^2 t$  and the long spatial scale  $X = \epsilon x$  and perturbing the steady state by  $(u, v)^\top = (E, B/E)^\top + \epsilon \mathbf{a} A(X, T) e^{ik_c x} + \epsilon \mathbf{c} C(X, T) e^{i\omega_c t} + c.c.$ , where  $\mathbf{a} = ((E^2 + k_c^2)/B_H, 1)^\top$ ,  $\mathbf{c} = (-E(E + i)/B_H, 1)^\top$ , and  $A(X, T)$  and  $C(X, T)$  are the complex amplitudes of the Turing and Hopf modes, respectively, the amplitude equations are readily calculated as

$$A_T = \zeta A_{XX} + \gamma A - g|A|^2 A - \lambda|C|^2 A, \quad (2.1a)$$

$$C_T = (\kappa_r + i\kappa_i)C_{XX} + \nu C - (\beta_r + i\beta_i)|C|^2 C - (\delta_r + i\delta_i)|A|^2 C. \quad (2.1b)$$

The constants in (2.1) are given in the appendix. All constants in (2.1) are real and, with the exception of  $\nu$  and  $\gamma$ , only functions of the parameter  $E$ . The coefficient  $\nu$  is given by  $\nu = \mu/2$ , while  $\gamma$  is a function of  $\mu$ ,  $\rho$ , and  $E$ . The conditions for supercriticality of the Turing and Hopf bifurcations are  $g > 0$  and  $\beta_r > 0$ , where the latter condition is always satisfied for the Brusselator model. A value of  $E$  for which the former

is satisfied is  $E = 1.4$ , which is the value used in all computations presented herein. For this value of  $E$  and  $\rho > 0$ , the bifurcation scenario is given in Figure 9(g) of [35]. The pure Turing mode stabilizes when  $\mu$  (and thus the amplitude of the pure Turing mode) is sufficiently large to suppress growth of the Hopf mode. This value of  $\mu$  can be readily computed from a linear stability analysis of (2.1). These weakly nonlinear results were used in the initial search for a pinning region in parameter space. We remark that four constants in (2.1) can be normalized by rescaling  $(A, C, X, T)$ . Though necessary for a complete analysis of (2.1), we choose not to carry out this normalization procedure in this paper for notational convenience.

### 3 Snaking Structure and Pinning Solutions

In this section, we first introduce the numerical procedure to be used to compute the pinning solutions. Both time evolution of the PDE system (1.1) and continuation for a system of ODEs (given in §3.1), gotten by representing the solutions by a finite number of Fourier modes, are employed. We then present the main results regarding the existence of a robust region in parameter space in which stationary striped structures and time periodic oscillations coexist in the same spatial domain. Such solutions vary continuously with the parameters of (1.1) and lie on snaking branches, each of which is characterized by a series of saddle-node bifurcations similar in appearance to the well known snaking structures found in studies of stationary pinning solutions. Two intertwined pairs of such solution branches are shown to exist. The main difference between solutions on these two pairs of branches is that on one pair, a defect is present at the center of the striped region, and on the other pair, no defect exists. Solutions on one branch of one pair differ from those on the other branch by a  $\pi$  phase shift in the spatially periodic region, i.e., locations of local minima (maxima) of solutions on one branch correspond to locations of maxima (minima) of solutions on the other branch. We discuss where these branches bifurcate, and describe the differences between solutions on different parts of each branch. For the non-defect pair of solutions, we discuss the depinning transition and wavelength selection. Lastly, we relate the results back to properties of the amplitude equations.

#### 3.1 Numerical Methods

We employ two approaches to numerically determine the bifurcation branches and the structure and stability of the solutions on those branches. In the first approach we solve the IBVP for the PDE system (1.1) and evolve the initial conditions to their eventual steady states. To determine the structure and stability of the solution branches, we employ AUTO, a continuation package which follows solutions along the various branches and determines their stability. The IBVP solver was used to 1) perform parameter searches to determine the parameters for pinning, and 2) provide appropriate initial guesses to be used in the AUTO computations. AUTO was then used to compute all the solution branches that we found and determine their stability.

We now describe the process by which we employed time evolution to compute pinning solutions. To locate the region in parameter space where pinning is possible, we first solved the IBVP system (1.1) with  $E = 1.4$  using a Fourier spectral method in space and a semi-implicit second order two step predictor-corrector method in time. The diffusion terms of (1.1) were treated implicitly while the reaction terms were treated explicitly. The latter were first computed in physical space before being transformed into Fourier space, where all time stepping was performed. The initial conditions for  $u$  and  $v$  were set as

$$(u, v)^\top = (E, B/E)^\top + \epsilon \text{Re} [a e^{ik_c x} \theta(x) + c(1 - \theta(x))] , \quad (3.1)$$

$$\theta(x) \equiv H(x + \ell/2) - H(x - \ell/2); \quad \ell < L ,$$

on a domain of length  $L$  subject to periodic boundary conditions, where  $H(x)$  is the Heaviside step function. Thus, the initial condition (3.1) contains a pure Turing mode on the interval  $[-\ell/2, \ell/2]$  and a pure Hopf mode on  $[-L/2, -\ell/2) \cup (\ell/2, L/2]$ . The  $u$  component of (3.1) is depicted in Figure 1(a). Note that the basic state of  $u$  is  $u = E = 1.4$ .

Fixing  $E = 1.4$  and setting  $\mu$  (equivalently,  $B$ ) sufficiently large as determined in §2 so that the pure Turing mode is stable, we varied  $\rho$  (equivalently,  $D$ ) until (1.1) yielded a time periodic solution marked by the coexistence of Turing and Hopf modes on the same spatial domain. The large time behavior of such a solution is depicted in the space-time plot in Figure 1(b), which shows a nearly stationary striped region embedded in a background of low wavenumber Hopf-like oscillations. Note that the locations of the interfaces between the Turing and Hopf regions remain constant in time. In all space-time plots, the spatial variable  $x$  is plotted on the horizontal axis, the temporal variable  $t$  is plotted on the vertical axis, and dark (light) regions indicate larger (smaller) values of  $u(x, t)$ . Space-time plots of  $v(x, t)$  simply appear as black-and-white inverted plots of  $u$ , and are thus not included.

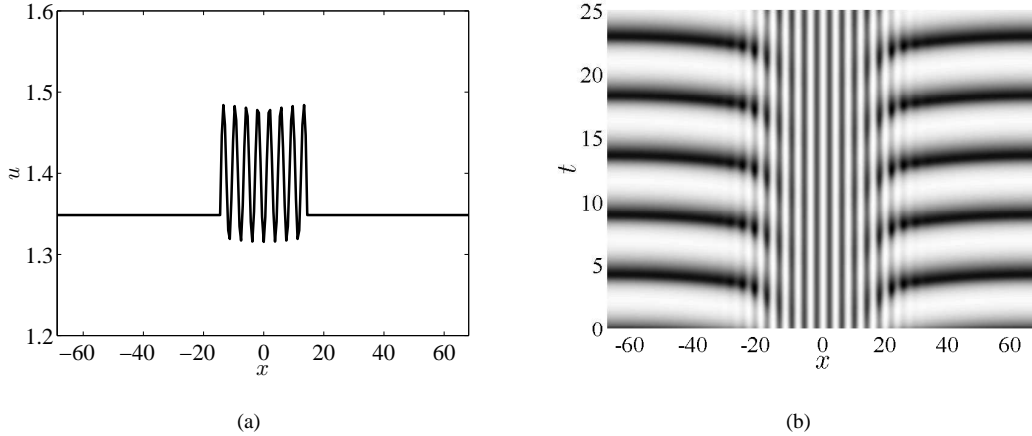


**Figure 1.** (a) Line plot of a typical initial condition of  $u$  for  $L \approx 137.37$ ,  $E = 1.4$ ,  $\epsilon = 0.1$ ,  $\mu = 25$ , and  $\rho = 0.178$  (equivalently,  $B = 3.21$ ,  $D \approx 0.2666$ ). (b) Space-time plot of  $u$  for large time starting from the initial condition in (a). Turing and Hopf modes coexist on the same spatial domain in a time periodic solution.

Most of the solutions shown in this section resemble an interval in time of Figure 1(b) consisting of one complete cycle of the oscillatory region. Analogous to the well studied problems in homoclinic snaking of stationary solutions, (1.1) admits an infinite multiplicity of solutions similar to Figure 1(b) that differ in the width of the striped region. While Figure 1(b) appears to be time periodic, all solutions that we have computed by means of time evolution have exhibited a slight aperiodicity, possibly due to the difference between the oscillation frequencies of the pure Hopf mode and the mixed mode between Hopf and Turing. However, time



periodic solutions do exist and can be found using AUTO, which was the main tool in obtaining the results reported in this paper.

One of the main capabilities of AUTO is the computation and continuation of limit cycles of systems of ordinary differential equations. To exploit this capability, we used AUTO to solve the time periodic BVP

$$\frac{1}{T} \frac{d\hat{u}_k}{dt} = -D \left( \frac{2\pi k}{L} \right)^2 \hat{u}_k + \hat{F}(u, v)_k, \quad \hat{u}_k(0) = \hat{u}_k(1), \quad k = 0, \dots, N, \quad (3.2a)$$

$$\frac{1}{T} \frac{d\hat{v}_k}{dt} = - \left( \frac{2\pi k}{L} \right)^2 \hat{v}_k + \hat{G}(u, v)_k, \quad \hat{v}_k(0) = \hat{v}_k(1), \quad k = 0, \dots, N, \quad (3.2b)$$

where  $\hat{f}_k$  denotes the amplitude of the  $k$ -th mode of the  $(N+1)$ -mode Fourier transform of  $f$ . In (3.2),  $F(u, v)$  and  $G(u, v)$  are the reaction terms on the right-hand sides of (1.1a) and (1.1b), respectively, and  $T$  is the period of the solution as determined by AUTO. As in the time stepping code, the reaction terms were computed first in physical space before being transformed into Fourier space. This formulation allowed use of the basic elements of the time evolution code described above, exploiting the fact that the IBVP solver directly computes the right-hand side of (3.2). The initial guess used to initialize the AUTO computations was the Fourier modes of  $u(x, t)$  and  $v(x, t)$  taken between the times  $t_0 \leq t \leq t_1$ , where  $u(-L/2, t_0)$  and  $u(-L/2, t_1)$  are both local maxima; in Figure 1(b), this condition corresponds to all slices in time between two consecutive horizontal black stripes, or between one complete oscillation of the Hopf mode. Here,  $u(x, t)$  and  $v(x, t)$  are solutions computed by time evolution. While, as noted previously,  $u(x, t_0)$  is not identical to  $u(x, t_1)$ , the aperiodicity is not so severe that AUTO is unable to converge onto a time periodic solution from the initial guess. Indeed, the solutions that AUTO computes are exactly periodic in time. We suspect that such time periodic solutions to (1.1) exist, though with an extremely small domain of attraction.

We make the following observations. First, in the example in Figure 1 with  $L \approx 137.37$ , results of the bifurcation diagram and solutions for  $u$  and  $v$  hardly changed as the number of Fourier modes was increased from  $N = 128$  to  $N = 256$ . Comparing two corresponding saddle-nodes in the snaking region, the value of  $D$  at the saddle-nodes differed in the two resolutions by less than 0.004%. Thus,  $N = 128$  was used in the computations. The length  $L$  was chosen so that exactly 36 wavelengths of a pure Turing solution with wavenumber  $k = k_c$  would fit in the domain. However, as we will show below, only 35 wavelengths are present when the solution is continued to a near-pure Turing state. Second, a pinning region in parameter space further into the nonlinear regime was documented in [26]. This regime was found to exhibit highly relaxational temporal oscillations that required a higher temporal resolution in AUTO to resolve. This was not conducive to this study, as the number of modes required to resolve the spatial variation already led to time-intensive computations. Further, results from AUTO indicate that solutions of the more nonlinear parameter regime may not be connected through the familiar snaking structure that will be presented in the next section for the weakly nonlinear regime. Lastly, the norm used as the measure of the solutions and plotted on the  $y$ -axis of the bifurcation diagrams below is given by

$$L_{2F} = \sqrt{\int_0^1 \sum_{k=0}^N [\hat{u}_k^2(t) + \hat{v}_k^2(t)] dt}. \quad (3.3)$$

The norm (3.3) is close to but not exactly equivalent to the  $L_2$  space-time norm, differing by a factor of two under the square root for  $k \neq 0$ . Also, since only even solutions are considered,  $\hat{u}_k(t)$  and  $\hat{v}_k(t)$  are real for all  $k$  and  $t$ .

### 3.2 Main Results

The complete bifurcation diagram of all solutions found is shown in Figure 2, where the diffusivity  $D$  is treated as the bifurcation parameter and plotted on the horizontal axis, and the norm (3.3) as the measure of the solutions plotted on the vertical axis. Heavy (light) segments indicate stable (unstable) solution branches. Representative solutions from each branch are shown in the figures below. We begin with a broad overview of each branch and discuss how they are located with respect to each other. We then describe each branch, and the corresponding solutions, in detail. We note that all branches and their solutions, stationary and time periodic, were computed by AUTO; different options were used to direct AUTO to compute each type of solution.

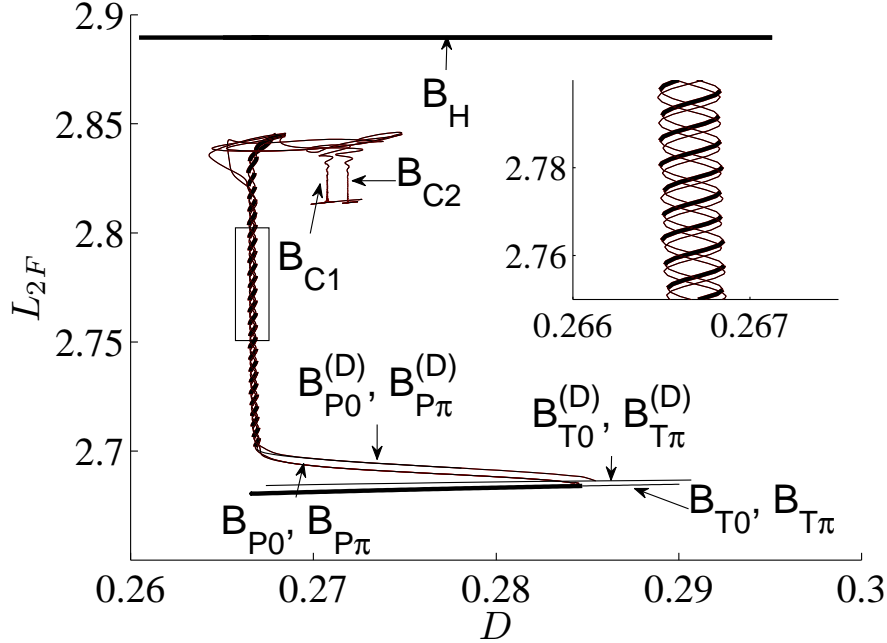


**Figure 2.** Complete bifurcation diagram for  $B = 3.21$ ,  $E = 1.4$ ,  $L \approx 137.37$ . The bottom two branches  $B_T$  and  $B_T^{(D)}$  are the stationary pure Turing and defect branches, respectively. The top branch  $B_H$  is the pure Hopf branch. The main snaking region on the left consists of two pairs of intertwined branches  $B_{P0}$  and  $B_{P\pi}$ , and  $B_{P0}^{(D)}$  and  $B_{P\pi}^{(D)}$ . Connected to these branches in the manner describe in Figure 5 are two distinct branches  $B_{C1}$  and  $B_{C2}$  exhibiting collapsed snaking behavior. The inset is a magnification of the main snaking region inside the rectangle.

Figure 2 includes two pure Turing branches  $B_{T0}$  (local maximum at  $x = 0$ ) and  $B_{T\pi}$  (local minimum at  $x = 0$ ), indistinguishable by the measure  $L_{2F}$ . These two branches arise from the rotational invariance of the solutions of (2.1a). In particular,  $A = \sqrt{(\gamma - \zeta k^2)/g} e^{i(kx + \phi)}$  ( $|k| \leq \sqrt{\gamma/\zeta}$ ) is a solution to (2.1a) for

any  $\phi$  when  $C = 0$ . However, within (1.1), the phases  $\phi = 0, \pi$  are the only ones that preserve the spatial reversibility symmetry. The stability transition on the pure Turing branches occurs at a Hopf bifurcation point at  $D \approx 0.28471$ . An analysis of (2.1) (not presented here as it is straightforward) predicts that, with  $\epsilon^2 = 0.01$  and  $\mu = 25$ , the transition occurs at  $D \approx 0.28531$ , a difference of approximately  $6 \times 10^{-4}$ . The point of stability transition also corresponds to the bifurcation point of the mixed mode. For clarity, we have plotted only a portion of the two pure Turing branches, and chosen not to plot the (unstable) mixed-mode branch. The pure Hopf branch, denoted by  $B_H$ , corresponds to the time periodic solution to (2.1b) with  $A = 0$ . The period of oscillations on the pure Hopf branch is  $T \approx 4.6623$ .

The two Turing-Hopf pinning branches  $B_{P0}$  and  $B_{P\pi}$  are connected through a saddle-node bifurcation near but not coinciding with the stability transition of the pure Turing branches. At this saddle-node point, the solution resembles solutions along the pure Turing branches  $B_{T0}$  and  $B_{T\pi}$ , with a small amplitude oscillation in time of period  $T \approx 4.4179$ . As is the case with all solutions described below, the period of oscillations is close to but not equal to the period of the pure Hopf oscillations. The space-time plot of the solution for  $u$  at the saddle-node, along with two line plots of two particular slices in time, are shown in Figure 3. While the length of the domain is able to accommodate exactly 36 Turing wavelengths of critical wavenumber  $k = k_c$ , only 35 are present in Figure 3. Hence among the discrete band of pure Turing solutions, each with a slightly different wavenumber allowed by the length of the domain, we have shown in Figure 2 only the two pure Turing branches for which there are 35 wavelengths corresponding to the same number as seen in Figure 3. This pattern can be shown to be Eckhaus stable by analyzing (2.1a) with  $C = 0$ .

The branches  $B_{P0}$  and  $B_{P\pi}$  continue towards decreasing values of  $D$  before beginning a snaking process in which the two branches intertwine. In the snaking region, the solutions on these branches resemble that of one temporal period of Figure 1(b). Because the  $L_{2F}$  norm of the pure Hopf branch is larger than that of the pure Turing branch, solutions higher up on the Turing-Hopf pinning branches  $B_{P0}$  and  $B_{P\pi}$  have a narrower striped region (i.e., fewer stripes) than those on the lower branches. Analogous to the distinction between the  $B_{T0}$  and  $B_{T\pi}$  branches, the two pinning branches are distinguished by solutions on  $B_{P0}$  having a local maximum at the center of the striped (Turing) region, and solutions on  $B_{P\pi}$  having a local minimum. The upward sloping segments in the snaking region are stable; all other solutions along the two branches are unstable.

Another pair of intertwined pinning branches,  $B_{P0}^{(D)}$  and  $B_{P\pi}^{(D)}$ , is also characterized by striped regions embedded in a background of Hopf-like oscillations. However, solutions on these two branches exhibit a defect in the central part of the striped region. All solutions along these two branches are unstable. In the same way that the branches  $B_{P0}$  and  $B_{P\pi}$  begin near a Hopf bifurcation point on the stationary pure Turing branch, the  $B_{P0}^{(D)}$  and  $B_{P\pi}^{(D)}$  branches begin near a Hopf bifurcation point on a pair of stationary defect branches  $B_{T0}^{(D)}$  and  $B_{T\pi}^{(D)}$  (indistinguishable by  $L_{2F}$ ). The space-time solution for  $u$  at the bottom of the  $B_{P0}^{(D)}$  branch is shown in Figure 4(a), while Figures 4(b) and 4(c) are line plots of  $u$  at two instants of time, indicating a slight temporal oscillation in the form of the spatial envelope. Figures 4(d) and 4(e) show time slices of the solution at the bottom of the  $B_{P\pi}^{(D)}$  branch, characterized by a local minimum, instead of a local maximum, at the center of the defect, centered at  $x = 0$ . Within the spatial envelope, 35 wavelengths are present. The stationary defect solutions on the  $B_{T0}^{(D)}$  and  $B_{T\pi}^{(D)}$  branches were described analytically in [17] in the framework of (2.1a) near a supercritical Turing bifurcation. As in the case of two branches of pure

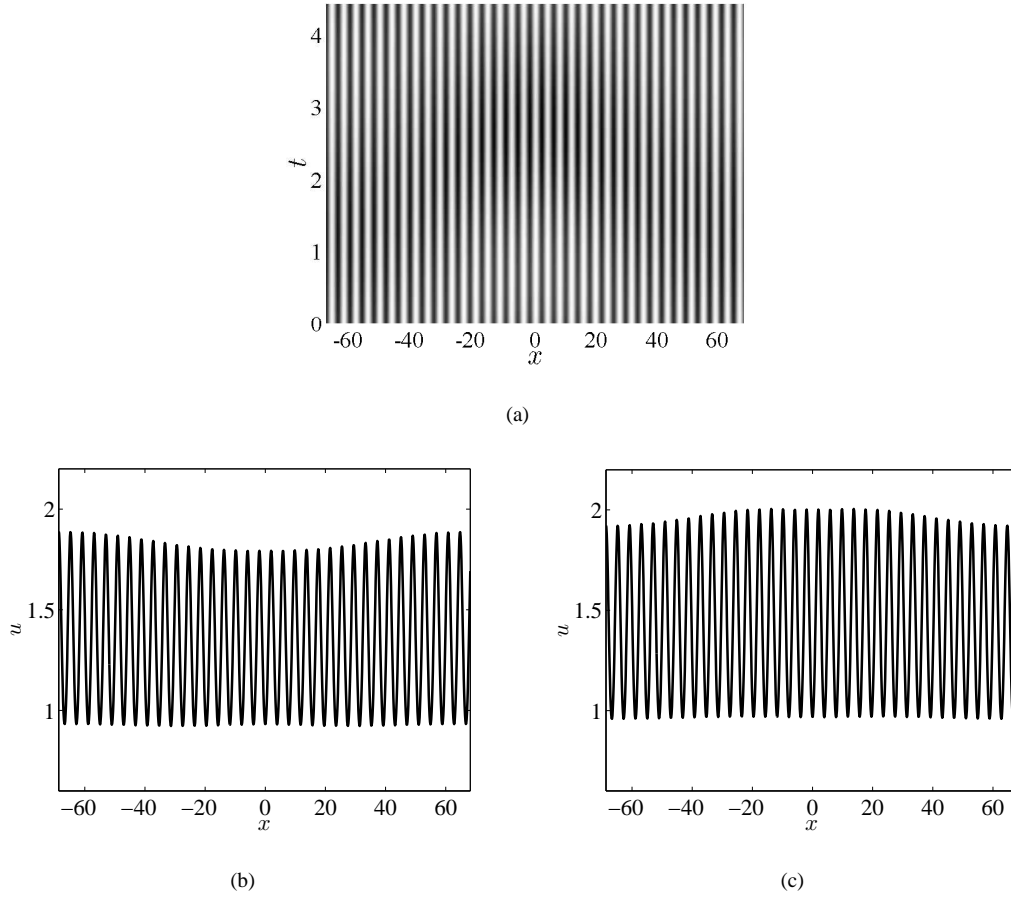


**Figure 3.** Shown in (a) is a space-time plot of  $u$  at the saddle-node bifurcation point of the two Turing-Hopf pinning branches  $B_{P0}$  and  $B_{P\pi}$ . The solution resembles a pure Turing solution with a small amplitude temporal oscillation of period  $T \approx 4.4179$  in the shape of the spatial envelope. The oscillations of the envelope can be inferred from (b) (time slice of (a) at  $t = 0$ ) and (c) (time slice of (a) at  $t \approx 2.1586$ ). The parameters are  $B = 3.21$ ,  $E = 1.4$ ,  $L = 137.37$ , and  $D \approx 0.2843$ . There are a total of 35 Turing wavelengths present.

Turing solutions, the stationary defect solutions have either a local minimum or maximum at the center of the defect.

Finally, to the right of the four snaking branches of pinning solutions are two separate branches  $B_{C1}$  and  $B_{C2}$  that exhibit properties similar to collapsed snaking (cf. [17] for stationary collapsed snaking), where the snaking region collapses to almost a single value in the bifurcation parameter. Solutions on these two branches consist of two regions in space of approximately antiphase pure Hopf-like oscillations separated by striped Turing-like structures. Solutions at different locations on each branch differ in the relative width of the two regions. A schematic of the connections between all branches discussed is shown in Figure 5.

All solutions on the branches described are even about  $x = 0$ . We have not been able to find any solutions that are odd. By time evolving (1.1) initialized with particular initial conditions on a periodic domain, we attempted to compute odd solutions in which two Hopf regions separated by two striped regions oscillate

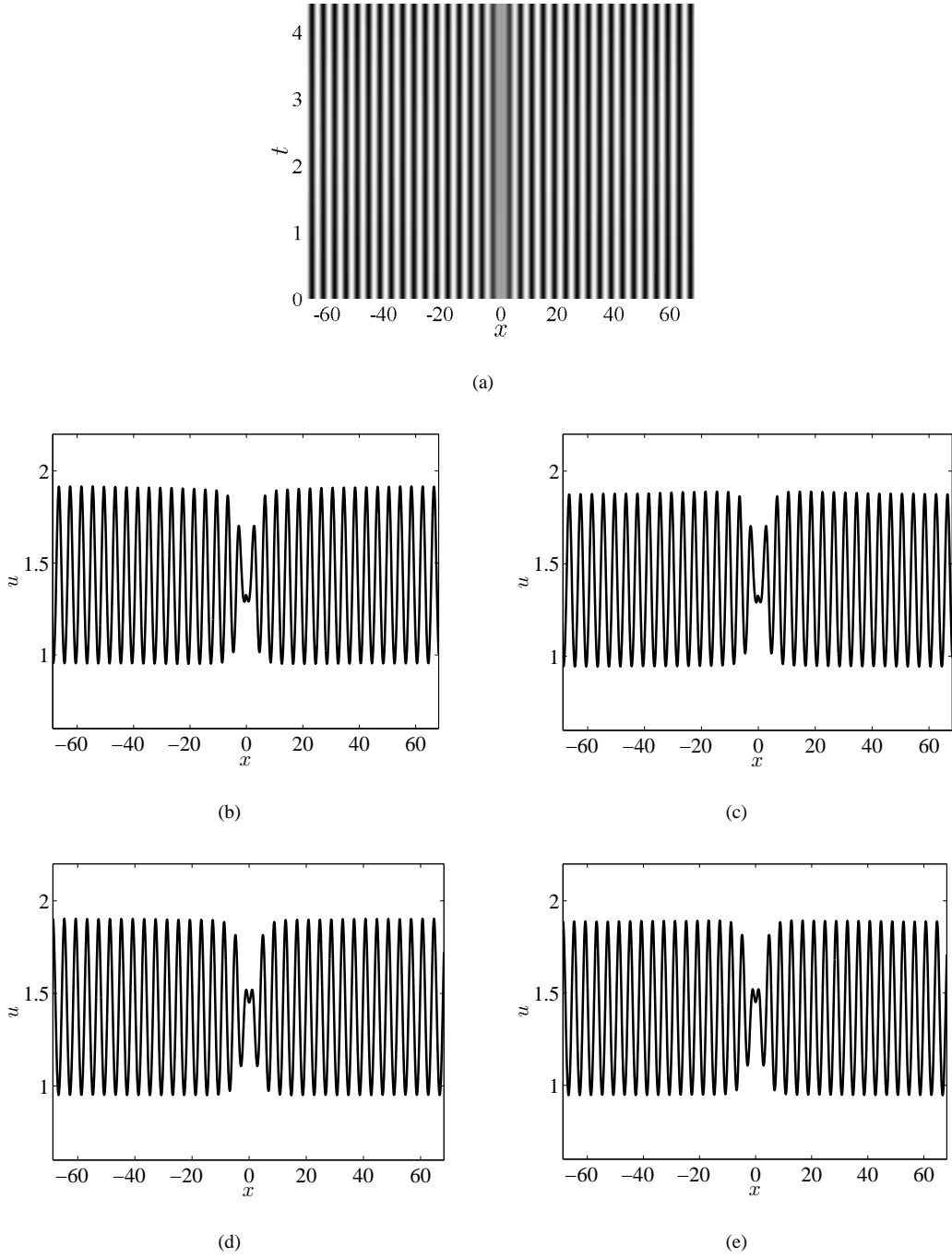


**Figure 4.** Solutions at the bottom of the  $B_{P0}^{(D)}$  and  $B_{P\pi}^{(D)}$  branches. The oscillations of the spatial envelope ( $T \approx 4.4167$ ) can be inferred from (b) (time slice of (a) at  $t = 0$ ) and (c) (time slice of (a) at  $t \approx 2.1991$ ) for the  $B_{P0}^{(D)}$  branch. Time-slices for the  $B_{P\pi}^{(D)}$  branch are shown in (d) and (e) ( $T \approx 4.4166$ ). The parameters are  $B = 3.21$ ,  $E = 1.4$ ,  $L = 137.37$ , and  $D \approx 0.28544$ . Within the spatial envelope, 35 wavelengths are present.

antiphase. However, due to the apparent presence of weak coupling of the Hopf regions through the striped regions, the initially antiphase oscillations synchronize over time. We were also unable to compute asymmetric solutions that, in the stationary pinning solutions of the Swift-Hohenberg equations (see e.g., [12] and [10]), make up the “rungs” that connect two intertwined snaking branches. Such solutions can be constructed by “gluing” together parts of solutions on one branch. However, when considering time periodic solutions, as we do here, each component must have the same temporal period, which is generally not the case. As a result, AUTO will not be able to converge to a time periodic solution. This is a fundamental difficulty with the present model, not encountered in previous studies of stationary pinning regimes.

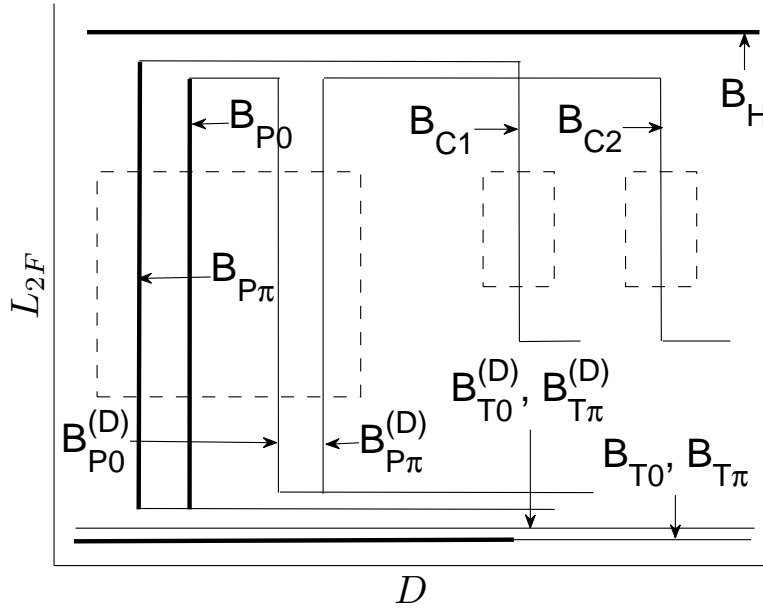


**Figure 5.** Schematic bifurcation diagram of Figure 2 illustrating connections between branches. The dashed boxes represent snaking regions. Dark segments indicate the existence of branches of stable solutions.

We now discuss each pair of branches in detail starting with the two pure Turing branches. In Figure 6, we show the solutions at the point of the stability transition where a Hopf bifurcation occurs, marked by a solid circle in Figure 6(a), on the branches  $B_{T0}$  and  $B_{T\pi}$ . The four pinning branches are also visible in Figure 6(a); in particular, the saddle-node point from which the  $B_{P0}$  and  $B_{P\pi}$  branches bifurcate can be seen to be located near the aforementioned Hopf bifurcation point on the pure Turing branches. Multiple Hopf bifurcation points occur on the  $B_{T0}$  and  $B_{T\pi}$  branches; the one marked by the solid circle located at the stability transition point is the one that occurs at the smallest value of  $D$ . The corresponding (stationary) solutions for  $u$  are plotted in Figure 6(b), which has a local maximum at  $x = 0$  ( $B_{T0}$ ) and Figure 6(c), which has a local minimum at  $x = 0$  ( $B_{T\pi}$ ). For clarity, only the interval  $x \in [-20, 20]$  is shown. The entire domain contains 35 wavelengths.

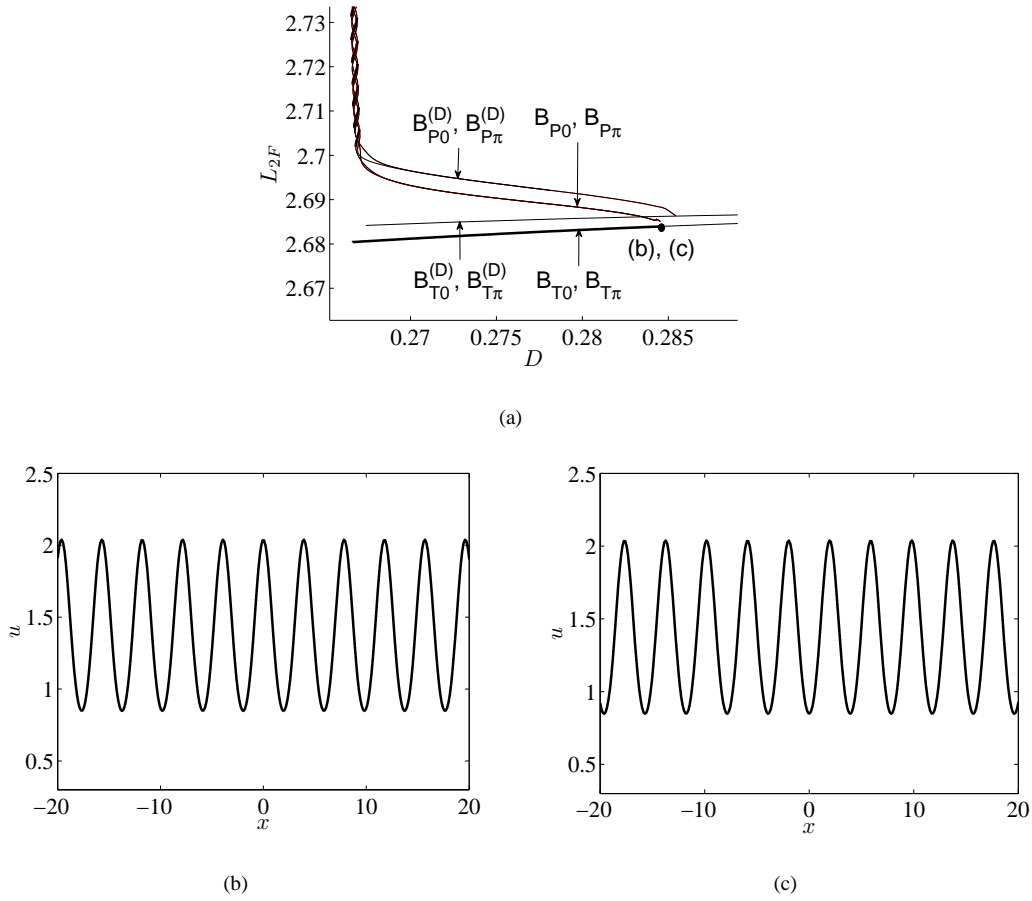


**Figure 6.** Closeup of stability transition point (indicated by solid circle) on the pure Turing branches (a) and the corresponding solutions for  $u$  on  $B_{T0}$  (b) and  $B_{T\pi}$  (c). The pure Turing branches are indistinguishable by the measure  $L_{2F}$ . The parameters are  $B = 3.21$ ,  $E = 1.4$ ,  $L \approx 137.37$ , and  $D \approx 0.2847$ .

As stated above, the two Turing-Hopf pinning branches  $B_{P0}$  and  $B_{P\pi}$  bifurcate from the saddle-node point located near the stability transition point of the two pure Turing branches  $B_{T0}$  and  $B_{T\pi}$ . In Figures 7(b) and 7(c), we show one space-time solution for  $u$  from the lower part of each branch to illustrate how the solutions on the branches differ from that of the saddle-node shown in Figure 3(a). Similarities between Figures 7(b) and 7(c) are immediate when spatial and temporal periodicity of the space-time plots are considered. This similarity is apparent when comparing Figure 7(c) to Figure 7(d), the latter of which has been periodically shifted in both space and time from Figure 7(b). The center of the striped region occurs at  $x = 0$  (or, by periodicity, the leftmost point in space of Figure 7(b)). In Figure 7(d), the center of the striped region is a local maximum (dark stripe) while in Figure 7(c), it is a local minimum (white stripe). These two solutions differ slightly both in the temporal period and the wavelength of the striped region. The mechanism(s) that affect these two quantities is an open problem. Experiments involving the time evolution of (1.1) suggest that the selection of the wavelength of the striped region is independent of initial conditions.

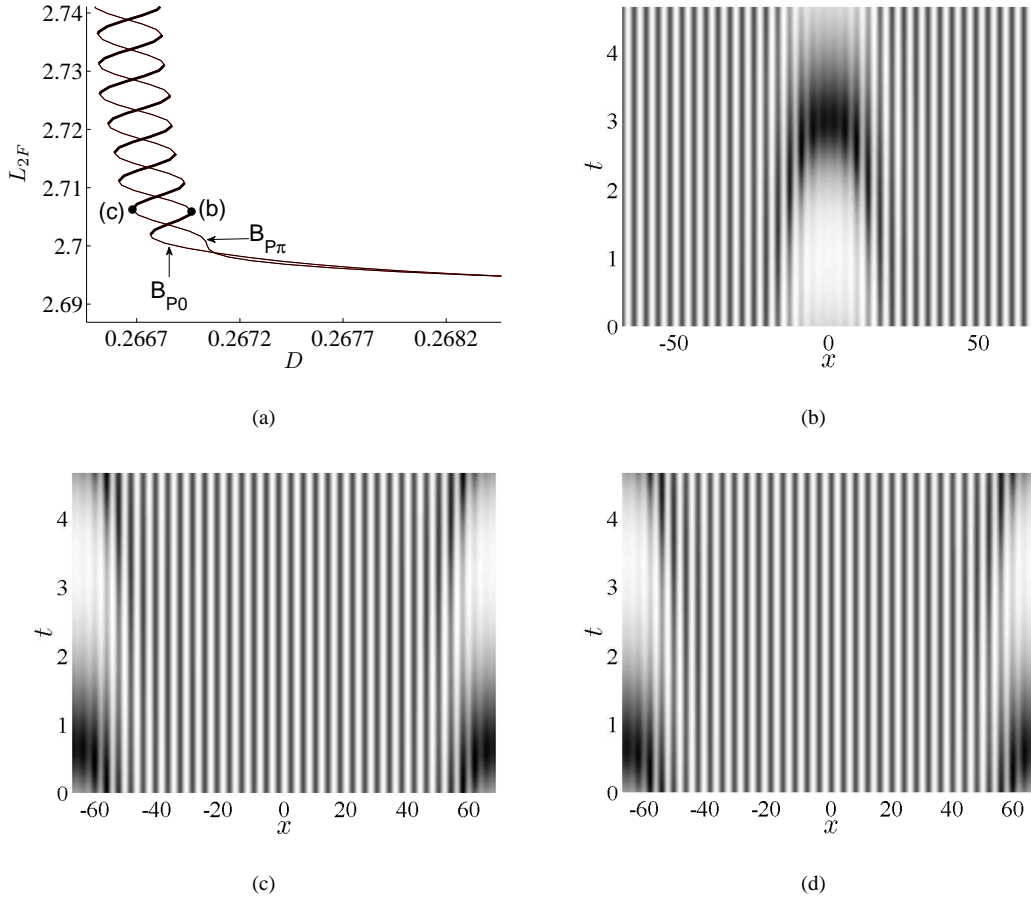


**Figure 7.** Solutions on the lower part of the Turing-Hopf pinning branches  $B_{P0}$  with  $D \approx 0.26702$  (b) and  $B_{P\pi}$  with  $D \approx 0.26673$  (c). The temporal periods are, respectively,  $T \approx 4.6450$  and  $T \approx 4.6452$ . In (d), we show a periodically (temporally and spatially) shifted plot of (b), illustrating the similarity between (b) and (c). The parameters are  $B = 3.21$ ,  $E = 1.4$ ,  $L \approx 137.37$ .

Snaking higher up the  $B_{P0}$  and  $B_{P\pi}$  branches, the spatial extent of the striped region is reduced through a series of saddle-node bifurcations. In Figure 8, we show the solutions at two saddle-nodes in the snaking region of the  $B_{P\pi}$  indicated in Figure 8(a) (the  $B_{P0}^{(D)}$  and  $B_{P\pi}^{(D)}$  branches have been removed for clarity). We note in Figure 8(a) that, while the saddle-nodes exhibit an approximate “lining-up property” (cf. [38]) where saddle-nodes occur at approximately the same value of the bifurcation parameter, we observe a nonmonotonic convergence of saddle-nodes in the parameter  $D$ , a departure from previous results on stationary snaking branches. The solution at the lower saddle-node, shown in Figure 8(b), is Turing-dominated while the one at the higher saddle-node, Figure 8(c), is Hopf dominated, consistent with the fact that in Figure 2, the stationary Turing branches have the smallest values of  $L_{2F}$  and the pure Hopf branch the largest. The periods of the solutions also differ slightly, with that of the solution higher on the branch closer to the period of the pure Hopf solution. While the number of stripes is difficult to quantify due to temporal oscillations and the interaction between Turing and Hopf regions, the process by which solutions gain or lose stripes can be clearly seen by comparing solutions at particular points in time.



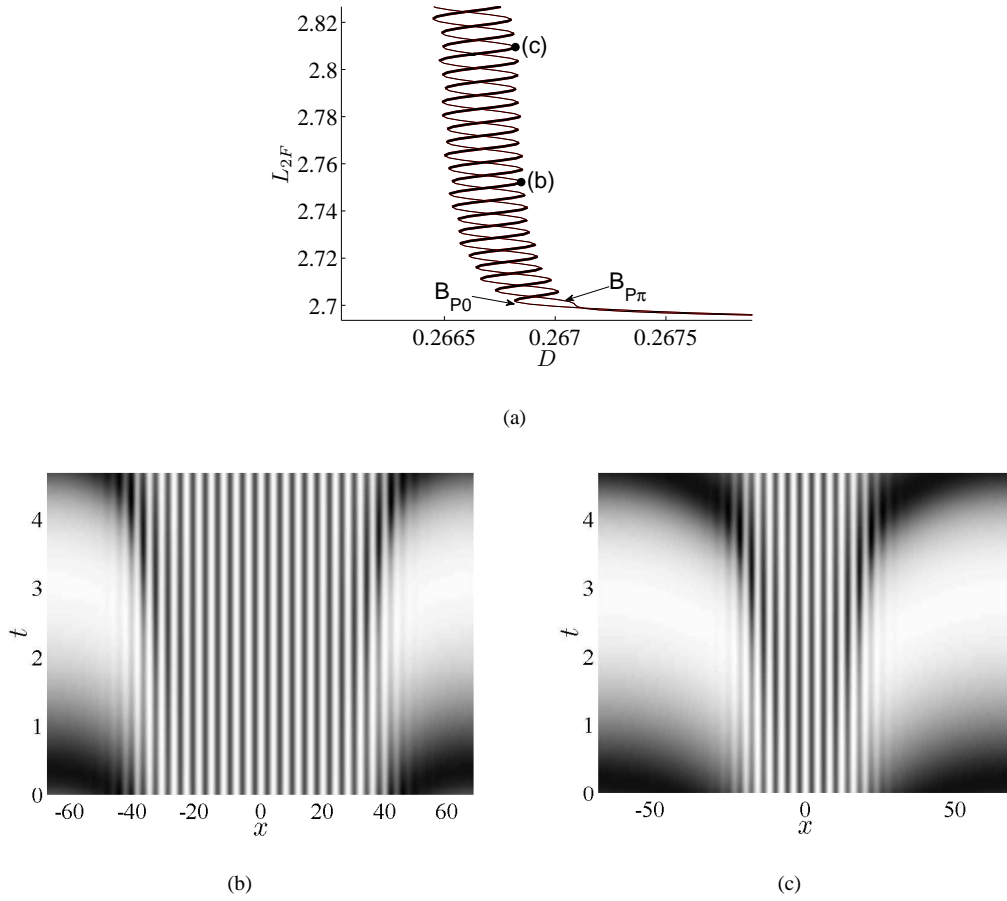


**Figure 8.** Progression of solutions along the snaking region (a) of the  $B_{P\pi}$  branch. For a solution on a low saddle-node (b), the striped region occupies the majority of the spatial domain, while for one on a high saddle-node (c), the time oscillatory region is dominant. The temporal periods of the solutions are  $T \approx 4.6573$  (b) and  $T \approx 4.6597$  (c). The parameters are  $B = 3.21$ ,  $E = 1.4$ ,  $L \approx 137.37$ ,  $D \approx 0.26685$  (b) and  $D \approx 0.26682$  (c).

In Figure 9 we show the process of the nucleation of a Turing cell, or stripe, as the  $B_{P\pi}$  branch is traversed downwards. In particular, for a typical segment of the snaking branch, we illustrate the difference between solutions at three consecutive saddle-nodes by plotting  $u(x, t_0)$ , where  $t_0 \in [0, T]$  is the instant in time when the center of the oscillatory region in  $u$  attains a local minimum in time. In Figure 9(a), we indicate the three saddle-node points of interest as well as two intermediate points. In Figure 9(b), the solution at saddle-node point (b) has a main Turing region containing 10 local maxima at which  $u$  has a value between 2 and 2.5. The main Turing region is bounded between two pairs of local maxima of lesser value. As the branch is traversed downwards, the two pairs of local maxima grow in amplitude, as seen in Figure 9(c), 9(d), 9(e), while very little is changed in the main Turing region. Once the saddle-node point (f) is reached (Figure 9(f)), the larger of the pair of maxima has grown to approximately equal height as the outer pair of maxima of the main Turing region. Thus, as the branch was traversed from saddle-node point (b) through saddle-node point (d) to saddle-node point (f), the main Turing region gained one pair of maxima, or two Turing wavelengths.

We make some remarks regarding the process illustrated in Figure 9. First, the mechanism of nucleation at the edge of the Turing region, including in particular the nucleation of two Turing wavelengths for every two saddle-nodes, is the same as that reported for the 2–3 Swift-Hohenberg equation in [14]. Second, comparing Figures 9(b) and 9(f) reveals that the larger the extent of the Turing region, the more the central stripes resemble that of the pure Turing stripes at the same value of  $D$ . This trend suggests that there is weak coupling between the two Turing-Hopf interfaces through the Turing region, and that the coupling strength weakens the greater the distance between the two Turing-Hopf interfaces. Third, all corresponding space-time solutions of Figures 9(b)–9(f) have slightly different temporal periods, given in the caption of Figure 9. Lastly, we observe the same nucleation characteristics for the defect pinning branches.

Solutions on the  $B_{T0}^{(D)}$  and  $B_{T\pi}^{(D)}$  branches are characterized by a spatially periodic pattern contained within a spatially varying envelope. Solutions on  $B_{T0}^{(D)}$  ( $B_{T\pi}^{(D)}$ ) have a local maximum (minimum) at  $x = 0$ . As indicated in Figure 10(a), both stationary defect branches are unstable. Multiple Hopf bifurcation points occur on the two branches; the one marked by the solid circle is the one that occurs nearest the bifurcation point of the defect Turing-Hopf pinning branches  $B_{P0}^{(D)}$  and  $B_{P\pi}^{(D)}$ . The two solutions at the Hopf bifurcation points are shown in Figures 10(b) and 10(c). Like the space-time solution at the bifurcation points of the  $B_{P0}^{(D)}$  and  $B_{P\pi}^{(D)}$  branches in Figure 4, 35 wavelengths are present inside the spatial envelope.

As seen in Figure 10(a), the defect Turing-Hopf pinning branches  $B_{P0}^{(D)}$  and  $B_{P\pi}^{(D)}$  begin near a Hopf bifurcation on the stationary defect branches  $B_{T0}^{(D)}$  and  $B_{T\pi}^{(D)}$ . The space-time solution at the bifurcation point is shown in Figure 4(a). The similarity between this solution and the stationary defect solution at the Hopf bifurcation point is immediate upon comparing Figure 4(b) to Figure 10(b) and Figure 4(d) to Figure 10(c). In Figure 11, we show two typical defect Turing-Hopf pinning solutions at low and high saddle-node points on the  $B_{P\pi}^{(D)}$  branch (Figure 11(a)). Other solution branches have been removed for clarity. The defect can be seen to be centered around  $x = 0$  in Figures 11(b) and 11(c). As with the non-defect pinning branches  $B_{P0}$  and  $B_{P\pi}$ , solutions lower on the branch have a larger striped region than those higher on the branch. The manner in which Turing wavelengths are nucleated on the branches  $B_{P0}$  and  $B_{P\pi}$  also applies to solutions on the defect pinning branches, and thus is not shown. We remark that although stationary defect pinning solutions have not been observed in the Swift-Hohenberg equations, they have been found in a periodically forced Ginzburg-Landau equation originally proposed in [39] and subsequently studied in detail in [40]. In this example the two “hybrid” snakes formed by defect pinning solutions coexist in the same snaking region as the two “primary” snakes formed by non-defect pinning solutions, precisely as in Figure 2. Besides, it was theoretically predicted in [40] that as the spatially periodic region of the pinning solution becomes wider along the snaking branches, the locations of the saddle-nodes on the two hybrid snakes approach their limiting values from the other direction and more slowly compared to those on the two primary snakes, which again agrees with the upper portion of Figure 2.

The collapsed snaking branches  $B_{C1}$  and  $B_{C2}$  lie to the right of the four main snaking branches described above. All solutions on the two branches are unstable. The  $B_{C1}$  branch connects to  $B_{P\pi}$ , and  $B_{C2}$  connects to  $B_{P0}^{(D)}$ , both through a complex array of saddle-nodes that will not be described here. A simplified schematic of these connections is shown in Figure 5. In Figure 12(a), we show a closeup of the two collapsed snaking branches. As the branch is traversed beginning from the top, the snaking region appears to collapse to a single value in  $D$  in a back-and-forth manner before broadening out at the bottom. Two typical solutions on the lower (Figure 12(b)) and upper (Figure 12(c)) part of the  $B_{C1}$  branch are shown. As either collapsed

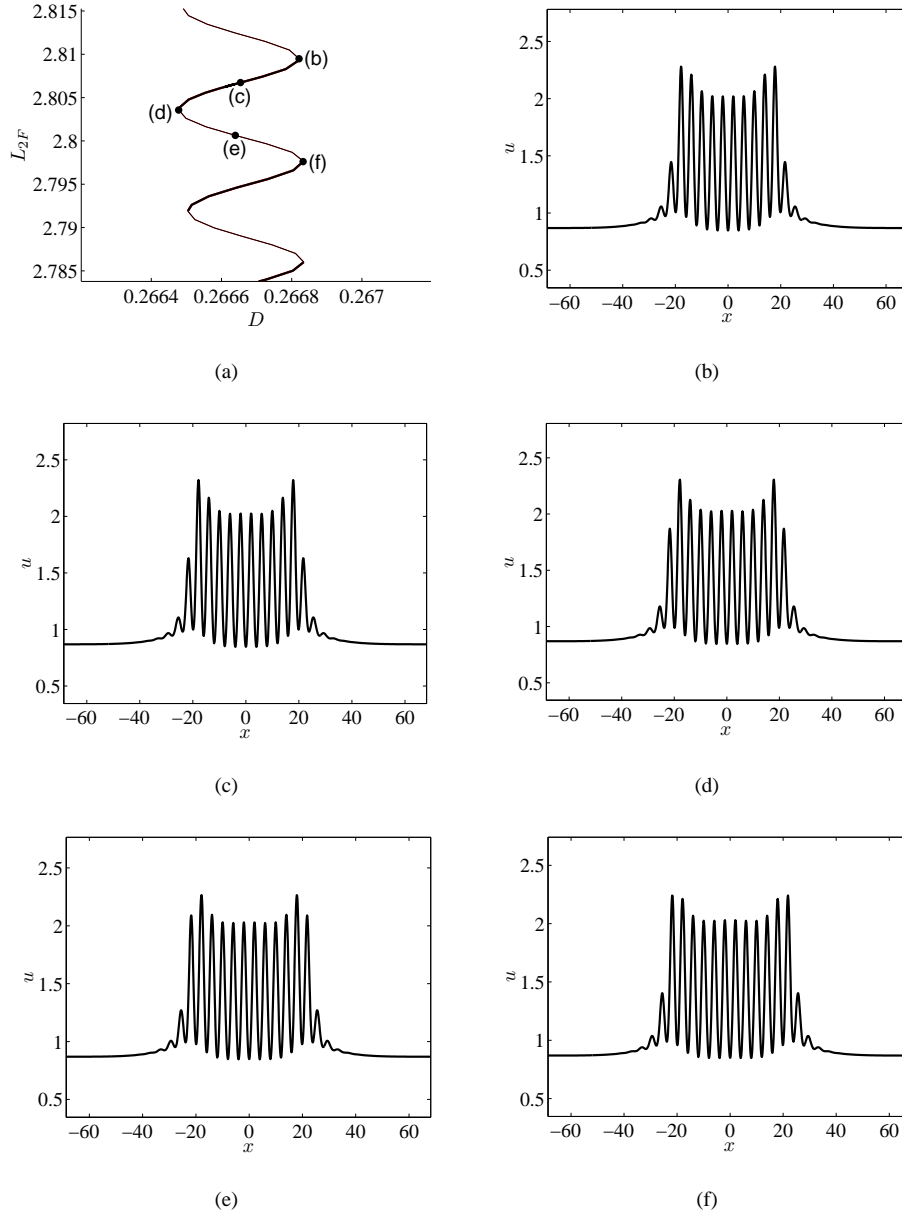


**Figure 9.** Illustration of the nucleation process that occurs at the edge of the Turing region. In (a), the locations on the  $B_{P\pi}$  branch of the subsequent figures are indicated. In the progression (b)–(f), the Turing region grows by a width of two wavelengths through the increase in amplitude of a pair of local maxima at its edges. The corresponding values of  $D$  and temporal periods of the solutions are  $D \approx 0.26682$ ,  $T \approx 4.6597$  (b),  $D \approx 0.26665$ ,  $T \approx 4.6597$  (c),  $D \approx 0.26648$ ,  $T \approx 4.6596$  (d),  $D \approx 0.26664$ ,  $T \approx 4.6595$  (e),  $D \approx 0.26683$ ,  $T \approx 4.6594$  (f). The parameters are  $B = 3.21$ ,  $E = 1.4$ , and  $L \approx 137.37$ .

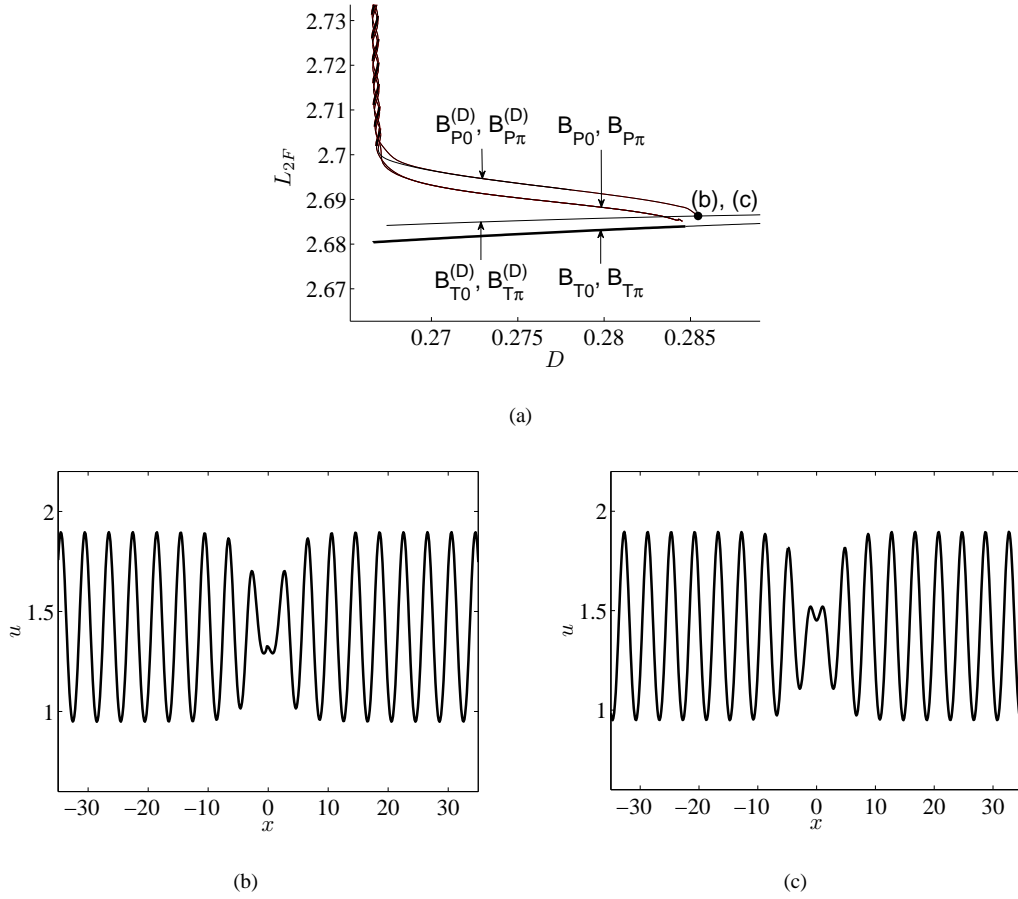


**Figure 10.** Closeup of the Hopf bifurcation point (indicated by solid circle) nearest the saddle-node bifurcation point of  $B_{P0}^{(D)}$  and  $B_{P\pi}^{(D)}$  on the stationary defect branches (a) and the corresponding solutions for  $u$  on  $B_{T0}^{(D)}$  (b) and  $B_{T\pi}^{(D)}$  (c). The stationary defect branches are indistinguishable by the measure  $L_{2F}$ . The parameters are  $B = 3.21$ ,  $E = 1.4$ ,  $L \approx 137.37$ , and  $D \approx 0.28544$ .

snaking branch is followed downward, the ratio between the widths of the Hopf region centered around the boundary and the one centered around  $x = 0$  decreases. This ratio becomes equal to 1 at the rightmost point of  $B_{C1}$  and the leftmost point of  $B_{C2}$ , which we will refer to as the symmetric point. After this point, the branch turns back onto itself on the bifurcation diagram and the width ratio continues to decrease. The solution at the symmetric point is invariant under a spatiotemporal flip, defined as a translation in  $x$  by half the domain size followed by a translation in  $t$  by half the Hopf period. In general the two solutions before and after the symmetric point at the same location on the bifurcation diagram are related to each other by the spatiotemporal flip. This solution behavior is in direct contrast to regular snaking discussed above in which solutions on lower and upper parts of the branch differed in the widths of the spatially periodic region, i.e., the number of Turing stripes. The fact that in the latter case, stripes are nucleated or destroyed as the branch is traversed, while in the former case, only the widths of predominantly spatially homogeneous structures are altered, offers a simple explanation for the fact that solutions such as those in Figures 12(b) and 12(c) lie on a collapsed snaking branch, while those in, e.g., Figure 8(b), lie on a snaking branch with finite width. The

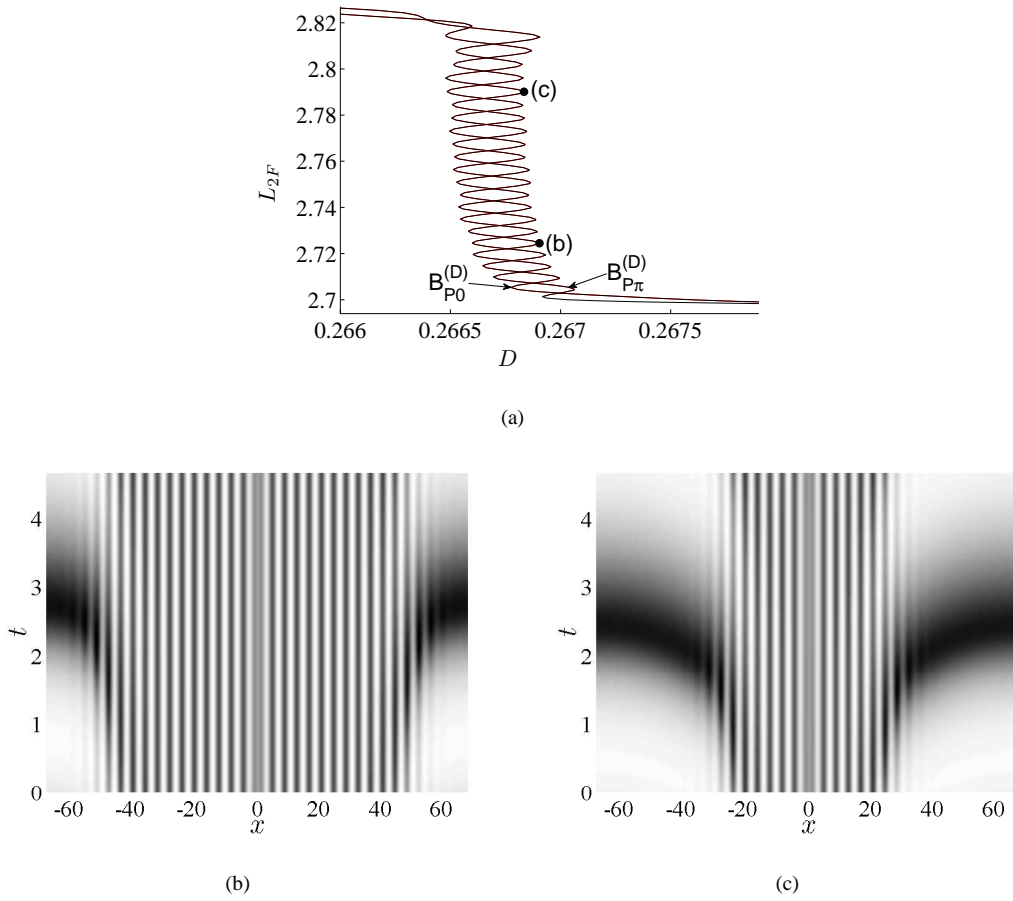


**Figure 11.** Progression of solutions along the snaking region (a) of the  $B_{P\pi}^{(D)}$  branch. For a solution on a low saddle-node (b), the striped region occupies the majority of the spatial domain, while for one on a high saddle-node (c), the time oscillatory region is dominant. The temporal periods of the solutions are  $T \approx 4.6533$  (b) and  $T \approx 4.6592$  (c). The parameters are  $B = 3.21$ ,  $E = 1.4$ ,  $L \approx 137.37$ ,  $D \approx 0.26690$  (b) and  $D \approx 0.26683$  (c).

difference between the solutions in Figure 12 and those on the other collapsed snaking branch  $B_{C2}$  will be illustrated below.

We make two remarks regarding Figure 12. First, the time oscillatory regions of space in Figures 12(b) and 12(c) are flatter than those of solutions described above (e.g., Figure 11(c)). Further, the frequency of these oscillations is closer to that of the pure Hopf frequency. These characteristics suggest that there is very little coupling between the time oscillatory regions and the interfaces in between them. Second, the nearly antiphase temporal oscillations in Figures 12(b) and 12(c) are separated by spatially oscillatory structures, while the corresponding branches in Figure 12(a) snake back and forth in their approach to a single value in the bifurcation parameter. A direct analog of this scenario for stationary solutions, where two spatially homogeneous states are connected by spatially oscillatory fronts, is given in [17]. There, the spatially oscillatory fronts were explained by the spatial eigenvalues of the two spatially homogeneous states. In this case, they form a quartet in the complex plane with nonzero real and imaginary parts, with the nonzero imaginary parts

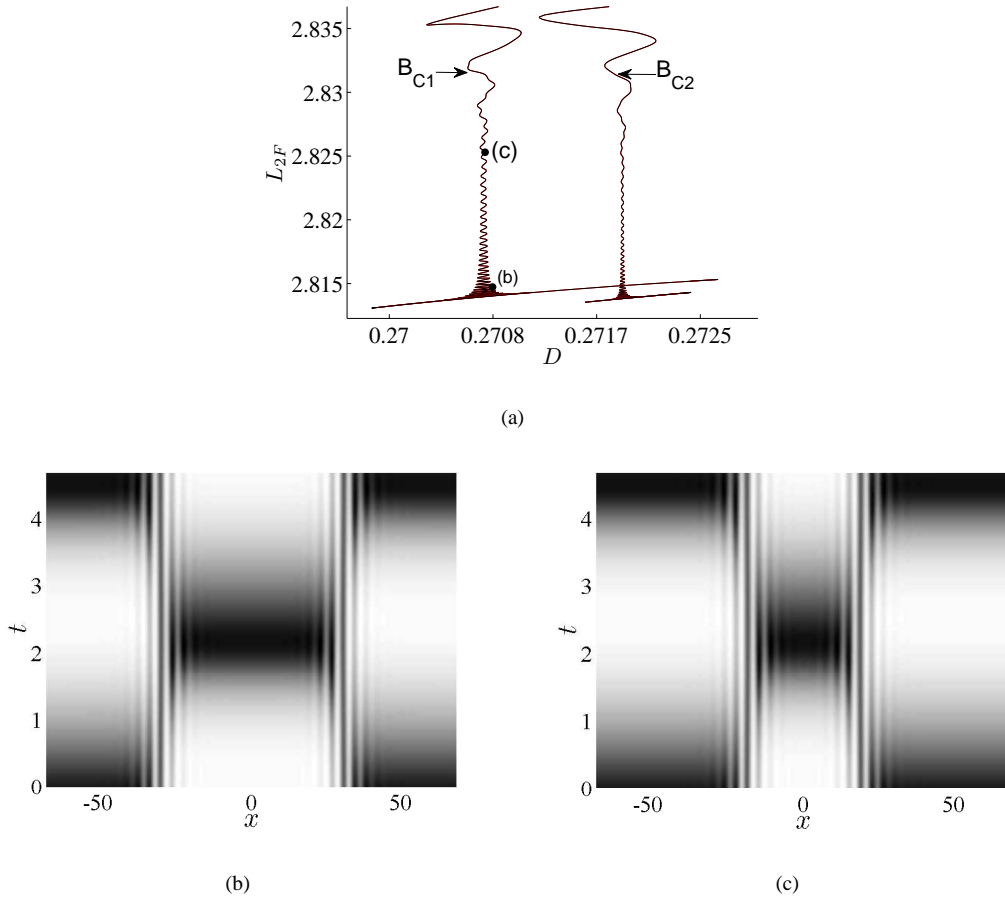


**Figure 12.** Progression of solutions along the collapsed snaking region (a) of the  $B_{C1}$  branch. The solutions in (b) and (c) (locations on the branch indicated in (a)) differ in the ratio between the widths of the time oscillatory regions. The temporal periods of the solutions are  $T \approx 4.66234$  (b) and  $T \approx 4.66231$  (c). The parameters are  $B = 3.21$ ,  $E = 1.4$ ,  $L \approx 137.37$ ,  $D \approx 0.27083$  (b) and  $D \approx 0.27077$  (c).

responsible for the spatially oscillatory front. For stationary solutions, the difference between regular snaking and collapsed snaking behavior has been understood as follows. Collapsed snaking solutions are explained in [41] as the intersection of the two-dimensional stable and unstable manifolds of two “stationary” (in space) states in a four-dimensional spatial dynamical system. This codimension one intersection is the reason behind the collapsed snaking structure of the solution branches; a slight perturbation in the value of the control parameter would lead to the breaking of the non-robust intersection of the manifolds. In contrast, the robust snaking region of regular snaking solutions can be explained by a codimension zero intersection between a two-dimensional unstable manifold of a stationary (in space) state with a three-dimensional center-stable manifold of a periodic orbit in space, with spatial reversibility guaranteeing the return orbit to the stationary state. Extension of this description to the present case of time dependent snaking behavior involves dimension counting in the style of [34] in the infinite-dimensional phase space of (1.1), and is left as future work.

In Figure 13(b), we illustrate the difference between two comparable solutions on the  $B_{C1}$  and  $B_{C2}$  branches, respectively. The solid curve shows the solution  $u(x)$  of Figure 12(b) at the time where  $u(0, t)$  is a local maximum. The dashed curve shows the same slice of a similar solution on the other collapsed snaking branch  $B_{C2}$ . The respective locations of the two solutions are shown in Figure 13(a). As has been the distinction between the 0 and  $\pi$  regular snaking branches, points in space where solutions on  $B_{C1}$  attain a local maximum (minimum) are approximately points where those on  $B_{C2}$  attain a local minimum (maximum). This antiphase relationship between the two collapsed snaking branches is not as exact as in the regular snaking branches, perhaps due to the separation of the collapsed branches in parameter space.

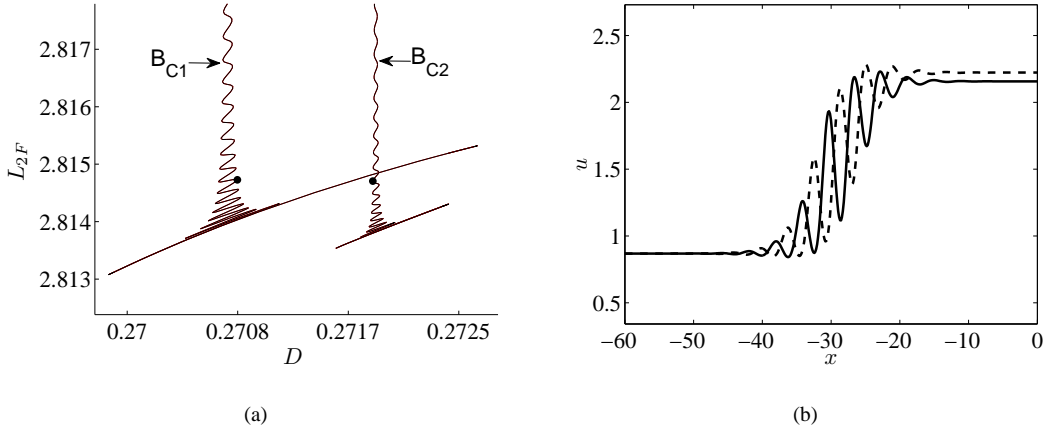


**Figure 13.** In (a), the bottom of the  $B_{C1}$  and  $B_{C2}$  branches are shown. In (b), two slices of space-time solutions on  $B_{C1}$  (solid) and  $B_{C2}$  (dashed) are shown. Their locations on the respective branches are indicated in (a) by solid circles. The spatially periodic regions of the two solutions oscillate approximately antiphase with periods  $T \approx 4.66234$  (solid) and  $T \approx 4.66229$  (dashed). The parameters are  $B = 3.21$ ,  $E = 1.4$ ,  $L = 137.37$  and  $D \approx 0.27083$  (solid) and  $D \approx 0.27185$  (dashed).

### 3.3 Depinning Transition

Within the regular snaking region described above, the solutions are time periodic and the relative widths of the striped and time oscillatory regions remain constant in time. That is, the Turing-Hopf front is pinned while the solution is inside the snaking region. Outside the snaking region, the fronts are expected to depin, as was the case for the 2–3 Swift-Hohenberg equation in [2]. The direction of depinning may be inferred from the weakly nonlinear analysis. In §2, we found that when  $\rho > 0$ , or equivalently  $D > D_c$ , the Hopf bifurcation occurs first as  $B$  is increased. This suggests that when  $D$  is increased, the Hopf mode becomes more dominant relative to the Turing mode. Thus, when  $D$  is set to the right of the pinning region, the Hopf region is expected to invade the striped region. Figure 14 illustrates the depinning dynamics that occur in this scenario. Figure 14(b) shows a space-time plot of  $u$  where the temporal oscillations have been removed for clarity by only recording times at which the center of the time oscillatory region attained a local minimum in time. As expected, the Hopf region (white) invades the striped region. The time evolution of (1.1) was

initialized with one slice in time of the space-time solution of  $u$  and  $v$  at a particular saddle-node as computed by AUTO. The parameter  $D$  was set at  $D = D_s + \delta$  with  $\delta > 0$ , where  $D_s$  is the value at the particular saddle-node marked by a solid circle in Figure 14(a). Invasion of the striped region was observed when the process was repeated with  $D$  set to the left of the snaking region (Figure 15).

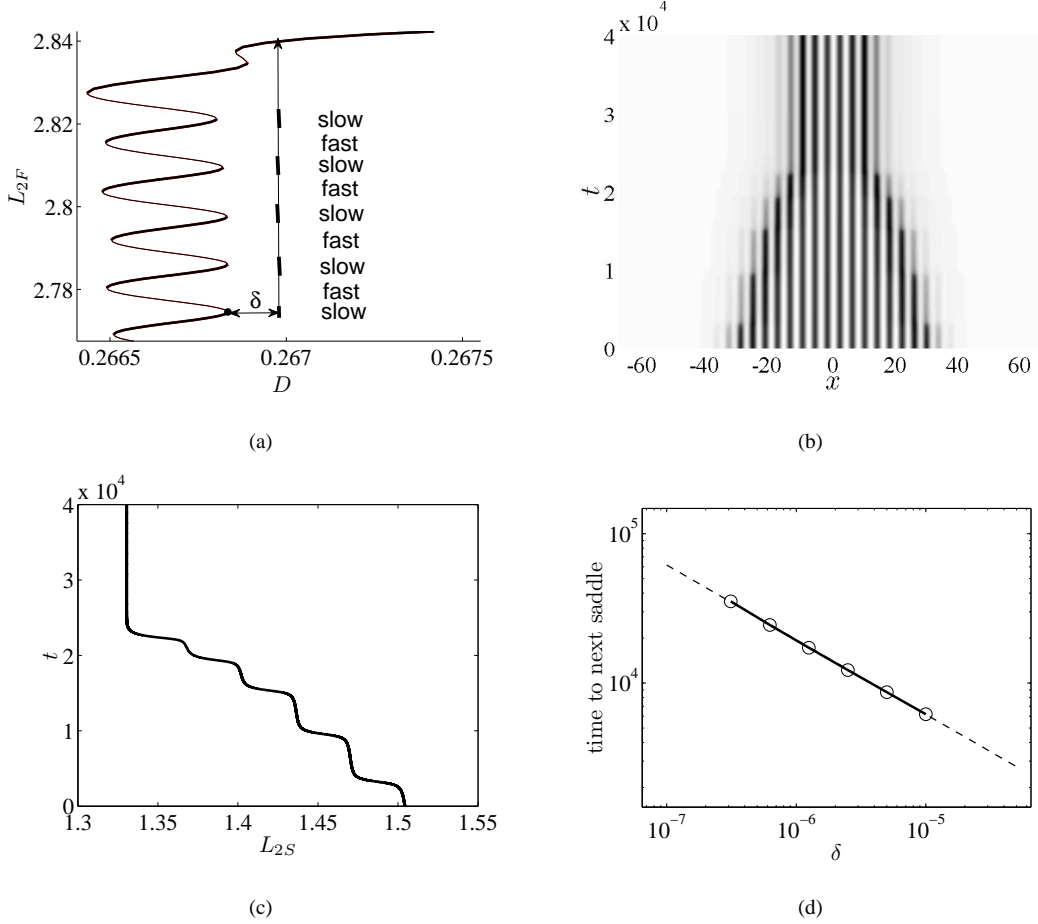


**Figure 14.** Shown in (a) is a closeup of the  $B_{P\pi}$  branch with the location of the initial condition indicated by the solid circle. At the saddle-node,  $D = D_s \approx 0.26683$ . The evolution up the branch at  $\delta$  distance outside the snaking region is depicted by the vertical arrow. The space-time depiction of the solution starting from this initial condition is shown in (b) for  $\delta = 1 \times 10^{-5}$ . Only the time slices at which the center of the time oscillatory region is at a local minimum are included. The slow-fast-slow evolution of  $L_{2S}(t)$  of the time slices of (b) is shown in (c) with time  $t$  on the horizontal axis. The corresponding slow and fast regions are indicated in (a). The  $\delta^{-1/2}$  scaling of the time of traversal between two saddle-nodes is shown in the log-log plot in (d). The solid line is a least squares fit through the data points (empty circles). The dashed line has a slope of  $-1/2$ .

The progression of the solution mirrors the depinning of stationary pinning solutions in [2]. Initialized in the neighborhood of a saddle-node, the solution evolves in a manner so as to approach the solution at the saddle-node either below it, if the striped state invades, or above it, when the Hopf state invades. This



progression can be inferred from Figure 8, as stripe-dominated solutions populate the lower portions of the branch. As in [2], we observe that the rate of evolution is slow in the vicinity of a saddle-node, increases away from the saddle-node, and decreases again near the next saddle-node. This slow-fast-slow progression past saddle-nodes has also been observed in nonlinear pulse splitting regimes (see e.g., [38, 42, 43]). Figure 14(c) illustrates the slow-fast dynamics by tracking the spatial norm  $L_{2S}(t)$  of each slice in time of Figure 14(b). The  $L_{2S}$  norm is defined as

$$L_{2S}(t) = \sqrt{\frac{1}{L} \int_{-L/2}^{L/2} u^2(x, t) dx}.$$

Note that, unlike the  $L_{2F}$  norm in (3.3),  $L_{2S}(t)$  decreases as the width of the striped region decreases. As seen in Figure 14(c), the norm decreases in a step-like progression in time, suggesting a sequence of destruction events separated by long intervals of relatively little change. Because the saddle-nodes do not line up exactly, times spent near each saddle-node are not uniformly distributed. We finally remark that the destruction events do not continue until the system reaches a pure Hopf state. This is due to the presence of stable branches that extend beyond the snaking region to the right, which can be seen in Figure 14(a) as well as in Figure 2. However, the progression of a Turing-Hopf pinning solution down the left side of the snaking region does evolve to a pure Turing state, seen in Figure 15(b). This is suggested by the snaking diagram shown in Figure 15(a). A wavelength adjustment occurs at  $t \approx 2 \times 10^4$  in Figure 15(b) so that the final state, like the pure Turing solutions described in §3.2, has 35 wavelengths.

Repeating the above procedure for various  $\delta$ , we observe that the time of traversal from one saddle-node to the next scales approximately as  $\delta^{-1/2}$ , the same scaling found in [2] for the 2–3 Swift-Hohenberg equation. This scaling was determined only by the time to traverse from the starting saddle-node, indicated in Figure 14(a) to the one immediately above it. We numerically determined the time by calculating the difference between the appropriate time slice  $u(x, t_0)$  of the solution computed by AUTO at the second saddle-node to every time slice of Figure 14(b). The time at which the  $L_{2S}$  norm of the difference was minimized was taken to be the time at which the solution was considered to have reached the second saddle-node. The log-log relation of the traversal time to the distance  $\delta$  from the saddle-node is shown in Figure 14(d); the solid line is a least squares fit through numerical data (empty circles), and the dashed line has slope  $-1/2$ . We finally remark that the aforementioned slight aperiodicity of the temporal oscillations in time evolved solutions of (1.1) makes it difficult to determine whether an integer number of temporal oscillations occur between saddle-node transitions. This difficulty is exacerbated by the vast difference in the time scales between one temporal period and the transition time.

### 3.4 Wavelength Selection

In studies of pinning solutions in the stationary Swift-Hohenberg equations, the wavelength of the periodic state was shown to vary within the snaking region. This variation can be understood by the conservation of a spatial Hamiltonian (cf. [44]), a property not available in the Brusselator model. However, in the latter case, the wavelength of the Turing state also varies within the snaking region and is distributed evenly among all stripes. We illustrate this phenomenon for solutions on the  $B_{P\pi}$  branch. Figure 16(a) shows a scatter plot of the wavelength of the striped region for solutions in the snaking region. It shows that, generally, the wavelength  $\lambda$  increases as the parameter  $D$  increases. Deviation from the trend near the top of Figure 16(a)

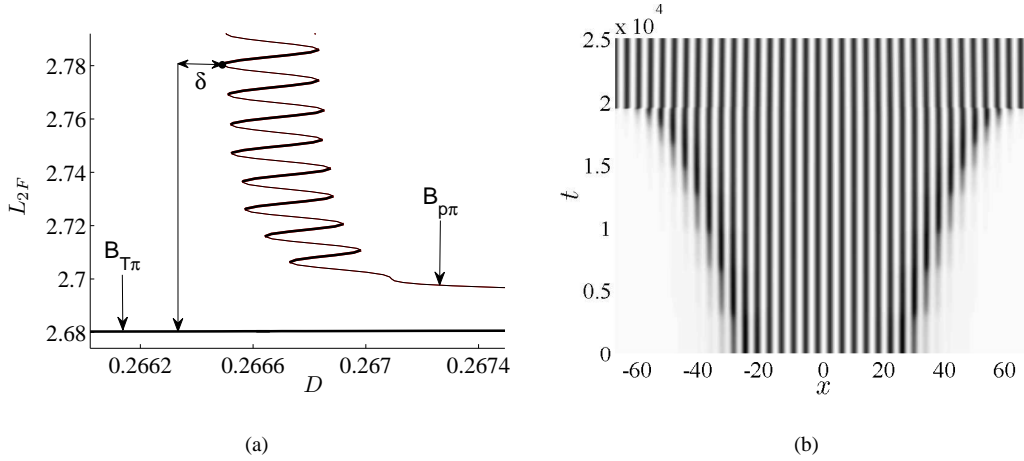


**Figure 15.** Shown in (a) is a closeup of the  $B_{P\pi}$  branch with the location of the initial condition indicated by the solid circle. At the saddle-node,  $D = D_s \approx 0.26649$ . The evolution down the branch at  $\delta$  distance outside the snaking region is depicted by the large vertical arrow. The space-time depiction of the solution starting from this initial condition is shown in (b) for  $\delta = -1 \times 10^{-5}$ . Only the time slices at which the center of the time oscillatory region is at a local minimum are included. A wavelength adjustment occurs at  $t \approx 2 \times 10^4$ . The final pure Turing state contains 35 wavelengths. The parameters are  $B = 3.21$ ,  $E = 1.4$ , and  $L = 137.37$ .

occurs for solutions near the top of the snaking branch. For those solutions, the Hopf region has significant influence on the entire striped region as a result of the Turing-Hopf coupling. For a typical solution, Figure 16(b) shows the  $x$  locations of each individual local maximum. The linear relationship implies a spatially uniform wavelength throughout the striped region. We note that the critical wavelength  $\lambda_c$  is  $\lambda_c \approx 3.8158$  and the value of  $D$  at the C2THP is  $D_c \approx 0.26483$ . Thus, Figure 16(a) shows that when  $D$  is closer to  $D_c$ , the wavelength  $\lambda$  is closer to  $\lambda_c$ . We also observe this trend with the parameter  $B$ ; the closer  $B$  is to  $B_H$ , the closer  $\lambda$  is to  $\lambda_c$ .

There is an important difference, however, between the wavelength selection in Figure 16(a) and that found for the (variational) 3–5 Swift-Hohenberg equation in [44]. In the case of the latter, the snaking region straddles a Maxwell point, a point of energy balance between the homogeneous and spatially periodic states. Deviation from the Maxwell point in the direction that favors the periodic state causes it to expand, resulting in a uniform increase in wavelength of the entire spatially periodic region. Further deviation beyond the snaking region triggers a depinning transition where the spatially periodic state invades the homogeneous state leading to a picture similar to Figure 15(b). The reverse is true when deviation from the Maxwell point energetically favors the homogeneous state. In this case, the picture would resemble Figure 14(b). Thus, the variation of the wavelength within the snaking region is consistent with the depinning process: when the bifurcation parameter is varied so as to increase the wavelength, further variation of the parameter in the same direction to outside the snaking region would lead to an invasion of the periodic state. Conversely, when the parameter is varied so as to decrease the wavelength, further variation to outside the snaking region would result in an invasion of the homogeneous state. This relation between wavelength selection and depinning

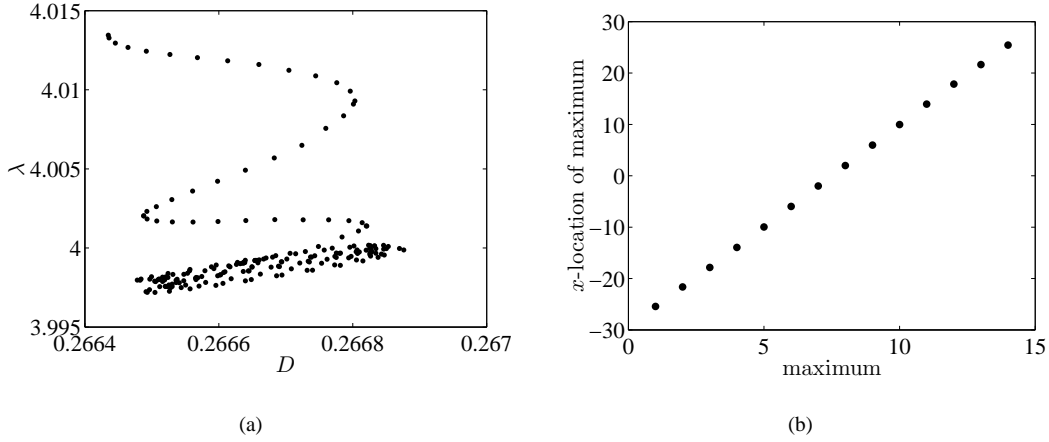


**Figure 16.** Shown in (a) is a scatter plot of the wavelengths  $\lambda$  of the striped region of solutions on the snaking segments of the  $B_{P\pi}$  branch. Most of the data points are concentrated in the lower region of the plot and suggest a positive correlation of  $\lambda$  with  $D$ . The approximately linear behavior shown in (b) of the locations of local maxima of a typical solution indicates equally spaced peaks and spatially uniform wavelengths. The parameters are  $B = 3.21$ ,  $E = 1.4$ , and  $L = 137.37$ .

direction does not apply in the case of the Turing-Hopf pinning solutions, however. Given the depinning results of §3.3, the reasoning above would suggest that the wavelength of the striped region should decrease (increase) when  $D$  increases (decreases). Figure 16(a) suggests that the opposite is true for the Turing-Hopf pinning solutions. Thus, the wavelength selection within the snaking region is unrelated to the direction of depinning. The latter is determined by the relative dominance between the Turing and Hopf modes and was explained in §3.3. An explanation for the former is given in the next subsection.

### 3.5 Comparison of Pinning Region to Results Based on Amplitude Equations

Like the Turing-Hopf pinning solutions described in §3.2 for the full Brusselator model (1.1), there also exist Turing-Hopf solutions of the amplitude equations (2.1). In such solutions as that in Figure 17(a), regions in space where  $(|A|, |C|) = (0, C_0)$  are connected by approximately exponential monotonic fronts (close up in Figure 17(b)) to regions where  $(|A|, |C|) = (A_0, 0)$ . We note that while  $|C|$  is stationary,  $C(x, t)$  is complex and oscillates periodically in time. The widths of the Turing and Hopf regions are arbitrary and thus a continuum of solutions exists for an appropriate parameter set. Such solutions of the amplitude equations translate to solutions similar to that shown in Figure 8 for the full Brusselator model. However, these solutions of the amplitude equations exist only on a codimension one subset in parameter space, while the snaking region of the Brusselator model is codimension zero. This point is developed further below. We remark that while Figure 17(a) resembles the mesa patterns constructed in [45] for a particular scaling of (1.1), that analysis does not appear to be applicable to (2.1).

Above,  $A_0 = \sqrt{\gamma/g}$  is the spatially homogeneous pure Turing amplitude, while the amplitude of the Hopf mode  $C_0 \approx \sqrt{\nu/\beta_r}$  is slightly affected by interaction with the Turing mode; its exact determination is beyond the scope of this paper. The reason that only the spatially homogeneous Turing amplitude needs to be considered is the property that the spatial dynamics of (2.1a) conserves a quantity in  $X$  (see e.g., [46])

that uniquely selects the wavelength. In particular, a solution  $A = R(X)e^{i\theta(X)}$  must conserve the “angular momentum”  $h(X) = R^2(X)d\theta/dX$ . If  $R(X) = 0$  for any  $X$ , then  $h(X) = 0$  for all  $X$ . Thus, at any point at which  $R(X)$  is nonzero,  $d\theta/dX = 0$  must hold, leading to a spatially homogeneous Turing region. By this conservation law, for any solution to (2.1) such that (2.1a) reaches a steady state, if there exists a region in space such that  $(|A|, |C|) = (0, C_0)$ , regions for which  $|C| = 0$  may only admit the spatially homogeneous  $A = A_0$  state. Indeed, when time evolving (2.1) initialized with  $A$  spatially periodic in the  $C = 0$  region, a coarsening of the Turing state occurs until the region is spatially homogeneous. This wavelength selection within the amplitude equations may explain the observation in §3.4 that the wavelength  $\lambda$  of the striped region is closer to the critical value  $\lambda_c$  the closer  $(B, D)$  are to  $(B_H, D_c)$ , their values at the C2THP.

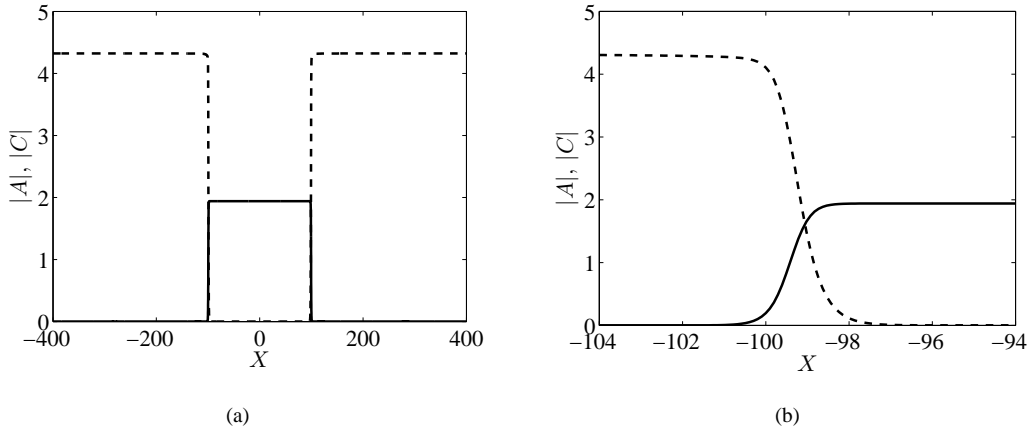


**Figure 17.** Shown in (a) is a plot of the stationary amplitudes of a Turing-Hopf solution of the amplitude equations. The Turing (Hopf) amplitude is the solid (dashed) line. The widths of the Turing and Hopf regions are arbitrary. The parameters are  $\mu = 25$ ,  $\rho = 0.1682$ , and  $E = 1.4$ . A close-up of the left front is shown in (b).

The front solution to (2.1) shown in Figure 17(a) only exists on a positively sloped line in  $(\mu, \rho)$ -space through the origin (dashed line in Figure 18(a)), a codimension one subset in parameter space. The  $\mu$ - $\rho$  relationship was obtained numerically by time evolving (2.1) for various  $\mu$  and  $\rho$  and observing pairs  $(\mu, \rho)$  for which the Turing-Hopf front remained stationary. The line shown in Figure 18(a) is a least squares fit through the computed data points (empty circles). We refer to this line as the Maxwell line, even though the problem is not variational. The significance of the Maxwell line is that the snaking region is expected to straddle the Maxwell line, regardless of whether the system is variational. Another nonvariational example can be found in [47], where a higher order analytical approximation to the Maxwell curve for stationary solutions of the (nonvariational) Lugiato-Lefever model was calculated from a seventh order Ginzburg-Landau equation near the codimension two point corresponding to weakly subcritical Turing bifurcation. This curve was shown to be straddled by a numerically determined snaking region of [24].

Below the Maxwell line in Figure 18(a), the Turing mode becomes less dominant in relation to the Hopf mode, and the Hopf mode invades the Turing mode. Above this line, the opposite is true. By comparing the Turing and Hopf growth rates  $\gamma$  and  $\nu$  given in the appendix, it is easily shown that the ratio  $\gamma/\nu$  decreases as

$D$  (or  $\rho$ ) increases. Unlike the full Brusselator model that has a codimension zero snaking region within the parameter space in which a continuum of solutions exist, the Turing-Hopf solutions of the amplitude equations only exist on a codimension one subset. The reason is that the amplitude equations do not capture the nonadiabatic effects of (1.1) responsible for the pinning of periodic fronts (see e.g., [1, 26, 47] and references therein), or equivalently, the broadening of the Maxwell curve. The black dots in Figure 18(a) are computed limits of the snaking region for various values of  $B$  for a domain length of  $L = 250$ . We observed that the limits of the snaking region shift more to the left, i.e., closer to straddling the Maxwell line, the larger the value of  $L$ . Comprehensive results for lengths significantly larger than  $L = 250$  were difficult to obtain due to computational constraints. Besides the length of the domain, another reason for the slight discrepancy may be the lowest order approximation of (1.1). In [47], it was shown that the weakly nonlinear analysis must be carried out to higher orders for the Maxwell curve to be straddled by the limits of the snaking region near a codimension two point. In Figure 18(b), we show a semi-log plot of the width of the snaking region in  $D$  for various values of  $-(B - B_H)^{-1}$ . The dashed line is a least squares fit through the data points (empty circles). The linear relation indicates that, near the C2THP, the width of the pinning region in  $D$  is exponentially narrow in  $-(B - B_H)^{-1}$ , consistent with the dominant part of the scaling analytically determined in [10]. The predicted scaling in [10] also contains an algebraic prefactor of the form  $(B - B_H)^{-2}$  in our notation, but we were unable to verify its presence based on the available data points.

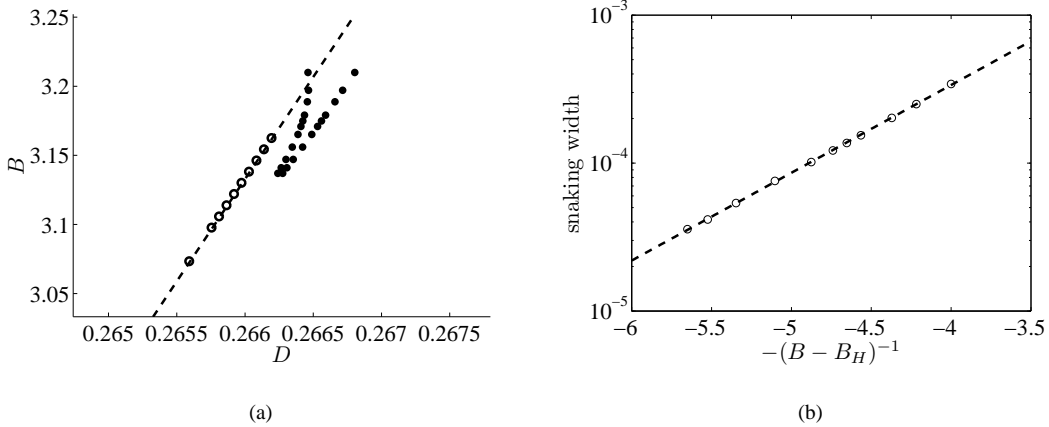


**Figure 18.** Figure (a) depicts the relationship between the numerically determined Maxwell line (dashed) and the limits of the pinning region (solid circles). The dashed line is a least squares fit through data points indicated by empty circles. The relationship between the Turing and Hopf growth rates  $\gamma$  and  $\nu$  on the Maxwell line is approximately linear, as can be seen from (a) along with the expressions for  $\gamma$  and  $\nu$  in the appendix. Figure (b) is a semi-log plot of the width of the snaking region in  $D$  as a function of  $-(B - B_H)^{-1}$ . For  $B$  near  $B_H$ , the width is approximately exponential in  $-(B - B_H)^{-1}$ .

## 4 Discussion

In this paper, we have extended the study of homoclinic snaking of stationary pinning solutions to solutions exhibiting time periodicity. Whereas most studies in the past have focused on the subcritical Turing regime of variational models, we have demonstrated snaking behavior near a C2THP of a nonvariational system where both the Turing and Hopf bifurcations are supercritical. In the region of Turing-Hopf bistability, we found multiple branches of solutions characterized by a coexistence of temporal oscillations and stationary stripes. By using AUTO to solve boundary value problems in time for the Fourier amplitudes of the space-time solutions, we were able to compute both stable and unstable solution branches. Two pairs of branches were found. Each solution on one pair contained a defect at the center of the striped region, while solutions on the other pair did not. The solutions on either pair of branches differ by a  $\pi$  phase shift in the spatially periodic pattern. We found that these branches displayed a similar structure to those found for stationary pinning solutions. Further similarities discovered include the manner in which striped structures of the space-time solutions were destroyed or nucleated when traversing up or down the branches. The scaling of the speed of the depinning transition with respect to distance from the nearest saddle-node was also found to be the same as that observed in studies of stationary pinning solutions. Lastly, within the framework of the amplitude equations valid near the C2THP, we numerically determined a Maxwell line, and showed that the pinning region was located nearby, with the separation decreasing as the length of the domain increased. There are, however, also important differences. The saddle-nodes of the snaking branches found did not monotonically converge to a single value in the bifurcation parameter. Also, instead of terminating on the pure Hopf branch the way that stationary pinning branches terminate on the homogeneous branches, the snaking branches found here connect to a pair of collapsed snaking branches through a series of complex saddle-nodes. Wavelength selection of the striped region along the snaking branches is also different. In particular, wavelength variation appears unrelated to the direction of depinning as was the case in the Hamiltonian spatial dynamics of the Swift-Hohenberg equations.

There are many open problems regarding Turing-Hopf pinning solutions near the supercritical C2THP of the Brusselator model. A qualitative interpretation, analogous to the spatial dynamics framework applied to the stationary pinning solutions, would provide valuable insights into the nature of the solutions found in this study. A quantitative determination of the  $\delta^{-1/2}$  scaling of the depinning time-scale has also not been attempted in this paper, due to the technical difficulties associated with asymptotic expansions around time-periodic pinning solutions. Other paths of analysis include calculating the Maxwell point of the system of amplitude equations, or extending the method of [10] to analytically determine the pinning region. A higher order system of amplitude equations may be derived to confirm that the corresponding higher order Maxwell line compares more favorably to the snaking region. The possibility of Turing-Hopf pinning solutions in higher spatial dimensions remains open for the Brusselator model, though Turing-Hopf coexistence in two dimensions near a supercritical C2THP has been numerically observed in [48] for a reaction-diffusion system describing semiconductor heterostructures. Stationary periodic Turing patterns in the two- and three-dimensional Brusselator model with regular diffusion were numerically computed in [49]. In [37], self-replicating localized spots and spots resulting from ring instabilities were observed numerically for the two-dimensional Brusselator model with superdiffusion. Stationary pinning solutions in higher spatial dimensions whose analogs could exist near a supercritical C2THP include radially symmetric (quasi-one-dimensional)

pinning solutions in the multi-dimensional Swift-Hohenberg equation [50], and fully two-dimensional pinning solutions in two-dimensional Swift-Hohenberg equations [51, 52].

Finally we mention several possible extensions of the present study. First, the numerical continuation method based on spatial Fourier transform can be readily adapted to compute the bifurcation diagrams of Turing-Hopf pinning solutions found by time evolution for the superdiffusive Brusselator model in [32]. However, the interpretation of pinning in terms of spatial dynamics might not be possible in this case. Second, the bifurcation structures of Turing-Hopf pinning solutions can become drastically different sufficiently far from the supercritical C2THP, when the snaking region interacts with bifurcations on either Turing or Hopf. In [40] it was shown that interaction of the snaking region with a saddle-center bifurcation on the spatially periodic state results in the primary and hybrid snakes reconnecting into a stack of figure-8 isolas. For the Turing-Hopf pinning branches, this type of reconnection is expected when the snaking region interacts with an Eckhaus bifurcation on the pure Turing branch. On the other hand, it is also possible for the Turing-Hopf snaking region to interact with many other types of bifurcations, including for example mixed-mode bifurcations and bifurcations of the Hopf periodic orbit in the temporal ODE. Third, the effect of noise on Turing-Hopf pinning solutions should be taken into account to facilitate comparison between the results presented in this paper and laboratory experiments. In [53] the dynamics of stationary pinning solutions in the 3–5 Swift-Hohenberg equation with an additive spatiotemporal Gaussian white noise were studied. It was shown that in the pinning region, the front velocity is the sum of a deterministic part which is the gradient of a sawtooth potential, and a stochastic part which is a temporal Gaussian white noise. In the absence of noise the front is trapped (or pinned) in the local minima of the sawtooth potential, but in the presence of noise the front moves (or depins) towards the global minimum of the sawtooth potential asymptotically in time. Hence the additive noise causes the front to propagate in a direction determined by the relative position to the Maxwell point. We expect similar dynamics for Turing-Hopf pinning solutions in view of the pinning region in the original PDE straddling the Maxwell point in the amplitude equation much like stationary pinning solutions, though in the Turing-Hopf case such dynamics cannot be readily interpreted in terms of stochastic gradient flows because both PDEs are generically nonvariational.

## Acknowledgements

This research was supported in part by NSF grants DMS 1007925 (JCT et al.) and DMS 0940261 (YPM).

## A Coefficients of Amplitude Equations

The coefficients of the amplitude equations in (2.1) are as follows:

$$\begin{aligned}\gamma &= -\frac{1}{2} \frac{E^2 (-\mu \sqrt{1+E^2} + \sqrt{1+E^2} E^2 \rho + \mu)}{(\sqrt{1+E^2} - 1)^2 \sqrt{1+E^2}}, \\ g &= -\frac{1}{18} \frac{(8 E^4 - 17 E^2 - 21 E^2 \sqrt{1+E^2} + 8 \sqrt{1+E^2} + 8) E^2}{(1+E^2) (\sqrt{1+E^2} - 1)^3}, \\ \lambda &= -\frac{(-17 E^6 + 4 E^6 \sqrt{1+E^2} + 27 E^4 \sqrt{1+E^2} - 43 E^4 - 40 E^2 + 32 E^2 \sqrt{1+E^2} - 16 + 16 \sqrt{1+E^2}) E^2}{(14 E^2 + 5 E^4 - 10 E^2 \sqrt{1+E^2} + 8 - 8 \sqrt{1+E^2}) (1+E^2)^{3/2} (\sqrt{1+E^2} - 1)},\end{aligned}$$

$$\begin{aligned}
\zeta &= 2 \frac{(\sqrt{1+E^2}-1)^2}{E^2+1-\sqrt{1+E^2}}, \\
\nu &= \frac{1}{2} \mu, \\
\beta_r &= \frac{1}{2} \frac{E^2+2}{1+E^2}, \\
\beta_i &= \frac{1}{6} \frac{4E^4-7E^2+4}{(1+E^2)E}, \\
\delta_r &= -\frac{(4E^6-33E^4\sqrt{1+E^2}+72E^4-94E^2\sqrt{1+E^2}+124E^2-56\sqrt{1+E^2}+56)E^4}{(14E^2+5E^4-10E^2\sqrt{1+E^2}+8-8\sqrt{1+E^2})(\sqrt{1+E^2}-1)^2(1+E^2)^{3/2}}, \\
\delta_i &= \frac{E^3(12E^6\sqrt{1+E^2}-44E^6+67E^4\sqrt{1+E^2}-94E^4+58E^2\sqrt{1+E^2}-58E^2-8+8\sqrt{1+E^2})}{(14E^2+5E^4-10E^2\sqrt{1+E^2}+8-8\sqrt{1+E^2})(\sqrt{1+E^2}-1)^2(1+E^2)^{3/2}}, \\
\kappa_r &= \frac{E^2+1-\sqrt{1+E^2}}{E^2}, \\
\kappa_i &= \frac{\sqrt{1+E^2}-1}{E}.
\end{aligned}$$

## References

- [1] Y. Pomeau, *Front Motion, Metastability and Subcritical Bifurcations in Hydrodynamics*, Physica D, **23**, (1986), pp. 3–11.
- [2] J. Burke, E. Knobloch, *Localized States in the Generalized Swift-Hohenberg Equation*, Phys. Rev. E, **73**, 056211 (2006).
- [3] E. Knobloch, *Spatially Localized Structures in Dissipative Systems: Open Problems*, Nonlinearity, **21**, (2008), T45–T60.
- [4] R. Richter, I. V. Barashenkov, *Two-Dimensional Solitons on the Surface of Magnetic Fluids*, Phys. Rev. Lett., **94**(18), 184503-1–4, (2005).
- [5] F. Haudin, R. G. Rojas, U. Bortolozzo, S. Residori, M. G. Clerc, *Homoclinic Snaking of Localized Patterns in a Spatially Forced System*, Phys. Rev. Lett., **107**(26), 264101-1–5, (2011).
- [6] P. D. Woods and A. R. Champneys, *Heteroclinic tangles and homoclinic snaking in the unfolding of a degenerate reversible Hamiltonian-Hopf bifurcation*, Physica D, **129**, (1999), pp. 147–170.
- [7] A. Bergeon, J. Burke, E. Knobloch, I. Mercader, *Eckhaus Instability and Homoclinic Snaking*, Phys. Rev. E, **78**, 046201 (2008).
- [8] S. M. Houghton, E. Knobloch, *Homoclinic Snaking in Bounded Domain*, Phys. Rev. E, **80**, 026210 (2009).
- [9] C. J. Budd, R. Kuske, *Localised Periodic Patterns for the Non-Symmetric Generalized Swift-Hohenberg Equation*, Physica D, **208**, (2005), pp. 73–95.
- [10] S. J. Chapman, G. Kozyreff, *Exponential Asymptotics of Localised Patterns and Snaking Bifurcations Diagrams*, Physica D, **238**, (2009), pp. 319–354.
- [11] H. Susanto and P. C. Matthews, *Variational approximations to homoclinic snaking*, Phys. Rev. E, **83**, 035201, (2011).
- [12] J. Burke, E. Knobloch, *Snakes and Ladders: Localized States in the Swift-Hohenberg Equation*, Phys. Lett. A, **360**, (2007), pp. 681–688.
- [13] A. D. Dean, P. C. Matthews, S. M. Cox, J. R. King, *Exponential Asymptotics of Homoclinic Snaking*, Nonlinearity, **24**, 3323 (2011).
- [14] J. Burke, *Ph.D. Thesis*, University of California, Berkeley, (2008).
- [15] P. Coullet, C. Riera, C. Tresser, *Stable Static Localized Structures in One Dimension*, Phys. Rev. Lett., **84**(14), (2000), pp. 3069–3072.
- [16] P. Coullet, C. Riera, C. Tresser, *Qualitative Theory of Stable Stationary Localized Structures in One Dimension*, Prog. Theor. Phys. **139**, (2000), pp. 46–58.
- [17] Y. –P. Ma, J. Burke, E. Knobloch, *Defect-Mediated Snaking: A New Growth Mechanism for Localized Structures*, Physica D, **329**, (2010), pp. 1867–1883.



- [18] A. Doelman, R. A. Gardner, T. J. Kaper, *Large Stable Pulse Solutions in Reaction-Diffusion Equations*, Indiana U. Math. J., **50**(1), (2001), pp. 443–507.
- [19] A. Doelman, W. Eckhaus, T. J. Kaper, *Slowly-Modulated Two-Pulse Solutions in the Gray-Scott Model I: Asymptotic Construction and Stability*, SIAM J. Appl. Math., **61**(3), (2000), pp. 1080–1102.
- [20] A. Doelman, W. Eckhaus, T. J. Kaper, *Slowly Modulated Two-Pulse Solutions in the Gray-Scott Model II: Geometric Theory, Bifurcations, and Splitting Dynamics*, SIAM J. Appl. Math., **66**(6), (2001), pp. 2036–2062.
- [21] A. Doelman, R. A. Gardner, T. J. Kaper, *Stability Analysis of Singular Patterns in the 1D Gray-Scott Model: A Matched Asymptotic Approach*, Physica D, **122**, (1998), pp. 1–36.
- [22] M. Beck, J. Knobloch, D. J. B. Lloyd, B. Sandstede, T. Wagenknecht, *Snakes, Ladders, and Isolates of Localised Patterns*, SIAM J. Math. Anal., **41**, (2009), pp. 936–972.
- [23] H. -C. Kao, E. Knobloch, *Weakly Subcritical Stationary Patterns: Eckhaus Instability and Homoclinic Snaking*, Phys. Rev. E, **85**, 026211 (2012).
- [24] D. Gomila, A. Scroggie, W. Firth, *Bifurcation Structure of Dissipative Solitons*, Physica D, **227**, (2007), pp. 70–77.
- [25] S. M. Houghton, E. Knobloch, *The Swift-Hohenberg Equation with Broken Cubic-Quintic Nonlinearity*, Phys. Rev. E, **84**, 016204 (2011).
- [26] A. De Wit, D. Lima, G. Dewel, P. Borckmans, *Spatiotemporal Dynamics Near a Codimension-Two Point*, Phys. Rev. E, **54**(1), (1996), pp. 261–271.
- [27] G. Nicolis, I. Prigogine, *Self-Organization in Nonequilibrium Systems*, Wiley, New York, 1977.
- [28] V. K. Vanag, *Waves and Patterns in Reaction Diffusion Systems. Belousov-Zhabotinsky Reaction in Water-in Oil Microemulsions*, Phys.-Usp. **47**, (2004), pp. 923–941.
- [29] B. Peña, C. Pérez-García, *Stability of Turing Patterns in the Brusselator Model*, Phys. Rev. E, **64**, 056213 (2001).
- [30] G. Heidemann, M. Bode, H. -G. Purwins, *Fronts Between Hopf- and Turing-Type Domains in a Two-Component Reaction-Diffusion System*, Phys. Lett. A, **177**, (1993), pp. 225–230.
- [31] P. Kolodner, *Coexisting Traveling Waves and Steady Rolls in Binary-Fluid Convection*, Phys. Rev. E, **48**(2), R665 (1993).
- [32] J. C. Tzou, A. Bayliss, B. J. Matkowsky, V. A. Volpert, *Interaction of Turing and Hopf Modes in the Superdiffusive Brusselator Model Near a Codimension Two Bifurcation Point*, Math. Model. Nat. Phenom., **6**(1), (2011), pp. 87–118.
- [33] E. J. Doedel, A. R. Champneys, T. Fairgrieve, Y. Kuznetsov, B. Oldeman, R. Paffenroth, B. Sandstede, X. Wang, and C. Zhang, *Auto07p: Continuation and Bifurcation Software for Ordinary Differential Equations*. Technical report, Concordia University, 2007.
- [34] B. Sandstede, A. Scheel, *Defects in Oscillatory Media: Toward a Classification*, SIAM J. Appl. Math., **3**(1), (2004), pp. 1–68.
- [35] H. Kidachi, *On Mode Interactions in Reaction Diffusion Equation with Nearly Degenerate Bifurcations*, Prog. Theor. Phys., **63**(4), (1980), pp. 1152–1169.
- [36] R. Wittenberg, P. Holmes, *The Limited Effectiveness of Normal Forms: A Critical Review and Extension of Local Bifurcation Studies of the Brusselator PDE*, Physica D, **100**, (1997), pp. 1–40.
- [37] A. A. Golovin, B. J. Matkowsky, V. A. Volpert, *Turing Pattern Formation in the Brusselator Model with Superdiffusion*, SIAM J. Appl. Math., **69**(1), (2008), pp. 251–272.
- [38] S. -I. Ei, Y. Nishiura, K. -I. Ueda,  *$2^n$ -Splitting or Edge-Splitting? - A Manner of Splitting in Dissipative Systems -*, Japan J. Indust. Appl. Math., **18**, (2001), pp. 181–205.
- [39] U. Bortolozzo, M. G. Clerc, S. Residori, *Local Theory of the Slanted Snaking Bifurcation Diagram*, Phys. Rev. E, **78**, 036214 (2008).
- [40] A. R. Champneys, E. Knobloch, Y.-P. Ma, T. Wagenknecht, *Homoclinic Snakes Bounded by a Saddle-Center Periodic Orbit*, SIAM J. Appl. Dyn. Sys. **11**(4), pp. 1583–1613, (2012).

- [41] J. Knobloch, T. Wagenknecht, *Homoclinic Snaking Near a Heteroclinic Cycle in Reversible Systems*, Physica D, **206**, (2005), pp. 82–93.
- [42] T. Kolokolnikov, M. J. Ward, J. Wei *The Existence and Stability of Spike Equilibria in the One-Dimensional Gray-Scott Model: The Pulse-Splitting Regime*, Physica D, **202**(3-4), (2005), pp. 258–293.
- [43] Y. Nishiura, D. Ueyama, *A Skeleton Structure of Self-Replicating Dynamics*, Physica D, **130**, (1999), pp. 73–104.
- [44] J. Burke, E. Knobloch, *Homoclinic Snaking: Structure and Stability*, Chaos, **17**, 037102 (2007).
- [45] T. Kolokolnikov, T. Erneux, J. Wei, *Mesa-type Patterns in the One-dimensional Brusselator and Their Stability*, Physica D, **214**, (2006), pp. 63–77.
- [46] R. Hoyle, *Pattern Formation: An Introduction to Methods*, Cambridge University Press, Cambridge, (2006).
- [47] G. Kozyreff, *Localized Turing Patterns in Nonlinear Optical Cavities*, Physica D, **241**, (2012), pp. 939–946.
- [48] W. Just, M. Bose, S. Bose, H. Engel, E. Scöll, *Spatiotemporal Dynamics Near a Supercritical Turing-Hopf Bifurcation in a Two-Dimensional Reaction-Diffusion System*, Phys. Rev. E, **64**, 026219 (2001).
- [49] A. De Wit, *Spatial Patterns and Spatiotemporal Dynamics in Chemical Systems*, Advances in Chemical Physics, **109**, (1999), pp. 435–513.
- [50] S. McCalla, B. Sandstede, *Snaking of Radial Solutions of the Multi-Dimensional Swift-Hohenberg Equation: A Numerical Study*, Physica D, **239**, (2010), pp. 1581–1592.
- [51] D. Avitabile, D. J. B. Lloyd, J. Burke, E. Knobloch, B. Sandstede, *To Snake or Not to Snake in the Planar Swift-Hohenberg Equation*, SIAM J. Appl. Dyn. Syst., **9**(3), (2010), pp. 704–733.
- [52] D. J. B. Lloyd, B. Sandstede, D. Avitabile, A. R. Champneys, *Localized Hexagon Patterns of the Planar Swift-Hohenberg Equation*, SIAM J. Appl. Dyn. Sys, **7**(3), (2008), pp. 1049–1100.
- [53] M. G. Clerc, C. Falcon, E. Tirapegui, *Additive Noise Induces Front Propagation*, Phys. Rev. Lett., **94**(14), 148302-1–4, (2005).